

Design Study of Belle II Interaction Region

Shinya Sugihara
Department of Physics, University of Tokyo

February 3, 2011

Abstract

The Belle II experiment will explore new physics beyond the standard model through the study of rare decay processes. The study will be performed at the asymmetric electron positron collider SuperKEKB which is designed to have a luminosity of $8 \times 10^{35} \text{ cm}^{-2} \text{s}^{-1}$.

To achieve this high luminosity, we have to design a new interaction region due to high background and reduced space in the interaction region. In this thesis, we discuss the possible solution for these design issues.

First, we estimate two beam backgrounds, Touschek and beam-gas background, expected at Belle II. To estimate the background levels, we performed a beam test at the current Belle detector.

Next, we test the cooling capability of the beam pipe by a mockup test. We discuss the two possible cooling schemes and their cooling capabilities. We also discuss selection of the coolant.

Finally, we perform a simulation study to understand the difference in tracking performance between two different SVD designs. The fixed-type mask design is dependent on the SVD design, and the choice of SVD design has important consequences for the IR design. This study is performed to support the design choice of the SVD.

Contents

1	Introduction	1
1.1	Belle-II, the Belle upgrade	1
1.2	Luminosity	2
1.3	Belle II detector	3
1.3.1	SVD/PXD	3
1.3.2	CDC	6
1.3.3	Particle identification(PID)	6
1.3.4	ECL	6
1.3.5	K_L^0 and μ detector (KLM)	6
1.4	Interaction Region(IR) issues	7
2	Estimation of beam background of SuperKEKB	9
2.1	Main background sources at SuperKEKB	9
2.2	Masks	11
2.3	Typical run of KEKB	12
2.4	Touschek study	15
2.4.1	Settings	15
2.4.2	Background estimation strategy	16
2.5	Estimation of background level of each detector	18
2.5.1	Estimation of $\tau_{\text{beam-gas}}$	18
2.5.2	Estimation of $k_{\text{beam-gas}}$ and k_{Touschek}	19
2.5.3	CDC	20
2.5.4	SVD/PXD	22
2.5.5	TOF/TOP	27
2.5.6	ECL	30
2.6	Conclusion	34
3	Cooling test of the beam pipe	35
3.1	The beam pipe design	35
3.2	Heat sources and requirement for cooling capability	37
3.3	Coolant selection	38
3.4	Requirement for cooling system	39
3.4.1	Pressure drop	39
3.4.2	Cooling capability	40

3.5	Setting for Cooling test	41
3.6	Viscosity of paraffin	42
3.7	Test of return cooling system	43
3.8	New beam pipe design	47
3.9	Conclusion	48
4	Tracking performance simulation study for SVD design	51
4.1	Slant and straight design	51
4.2	Tracking resolution simulation with fast simulation	54
4.2.1	TRACKERR simulation	54
4.2.2	Helix parameters	54
4.2.3	Effect on particle through matters	55
4.2.4	Intrinsic resolution	56
4.2.5	Input parameters	56
4.2.6	Simulation check	58
4.2.7	Effect of paraffin coolant	59
4.2.8	Estimation of vertexing and tracking performance	59
4.3	Comparison with the result of 2004	61
4.4	Summary	62
5	Conclusion	64
A	Miscellaneous topics about Touschek study	66
A.1	Mask setting dependence	66
A.2	Beam current dependence	66
A.3	Number of bunch dependence	67
B	Vacuum bump study	70
B.1	Beam gas background at the IP	70
B.2	Vacuum bump study at upstream of the IP	70
C	KEKB beam background simulation check	75
C.1	KEKB simulation for Touschek and beam-gas background estimation.	75
C.2	SVD occupancy measurement	76
C.3	Results	76

List of Tables

1.1	Beam parameters of KEKB and SuperKEKB. Parameters of KEKB are achieved value [1].	3
1.2	Expected performance of sub-detectors of Belle II.	5
2.1	Machine parameters of Exp.61 run1053.	14
2.2	Summary of Touschek study. V-close means vertical masks are closed and horizontal masks are open. H-close means vertical masks are opened and horizontal masks are closed. Both open means both vertical and horizontal masks are opened.	15
2.3	$k_{\text{beam-gas}}$ and k_{Touschek} for CDC current and expected CDC cur- rent if we put the same CDC at the same place as Belle under the conditions of SuperKEKB.	21
2.4	Configuration of the Belle II CDC sensor wires.	22
2.5	$k_{\text{beam-gas}}$ and k_{Touschek} for SVD hit and expected SVD hit if we put the same SVD at the same place as Belle under the conditions of SuperKEKB.	25
2.6	Detector configuration of the Belle II SVD, the radius of the straight part (not slanted), and strip number of the p-side (par- allel to the z axis), and n-side (perpendicular to the beam axis).	26
2.7	$k_{\text{beam-gas}}$ and k_{Touschek} for SVD hit(> 3000 electron-hole) and expected SVD hit if we put the same SVD at the same place as Belle under the conditions of SuperKEKB(> 3000 electron-hole).	27
2.8	$k_{\text{beam-gas}}$ and k_{Touschek} for TOF hit rate and expected TOF hit rate if we put the TOF at the same place as Belle under the conditions of SuperKEKB.	29
2.9	$k_{\text{beam-gas}}$ (column 1) and k_{Touschek} (column 2) for ECL energy deposit (HER). Expected ECL energy deposit from HER when we put the same ECL at the same place as Belle under the conditions of SuperKEKB (column 3). Expected energy deposit at each crystal of the Belle II ECL with wave form fitting and shorter shaping time at each region assuming uniform energy deposit to all crystals (column 4).	31

2.10	$k_{\text{beam-gas}}$ (column 1) and k_{Touschek} (column 2) for ECL energy deposit (LER). Expected ECL energy deposit from LER when we put the same ECL at the same place as Belle under the conditions of SuperKEKB (column 3). Expected energy deposit at each crystal of the Belle II ECL with wave form fitting and shorter shaping time at each region assuming uniform energy deposit to all crystals (column 4).	32
2.11	Background of each sub-detector in Exp.61 and expected background at SuperKEKB using the current Belle detector under the conditions of SuperKEKB.	34
3.1	Physics properties of beam pipe material. Aluminum is used for the beam pipe mockup.	36
3.2	Physics properties of various coolants.	38
3.3	Measurement of viscosity of paraffin. Measurement error is considered.	43
3.4	The heat paraffin obtained through the mockup(Q) for each flow rate and temperature. The heat source is 80 W.	47
3.5	Material for the straight part of the beam pipe from innermost to outermost. Inner radius is 10 mm and total thickness is 2 mm. Paraffin gap of the one-way system is smaller than that of the return cooling system.	48
3.6	Expected performance of return and one-way cooling system. . .	50
4.1	Atomic number, radiation length and effective thickness of each component(X/X_0). PF200 is the coolant used in CLEO which may have similar physics property to the paraffin used in the Belle system	56
4.2	The dr and dz resolution of 2004 and 2010 result.	62
B.1	Summary of vacuum bump study.	71
C.1	Parameters for the simulation and the beam test	77
C.2	Occupancy of each SVD layer (1-3) estimated by simulation and measured.	78

List of Figures

1.1	Side view of Belle II (top half) and Belle (bottom half) detector for comparison.	4
1.2	Schematic layout of the interaction region of Belle(top) and Belle II(bottom).	8
2.1	The location of movable masks in the KEKB ring.	12
2.2	The location of movable masks in the beam lattice diagram (LER of KEKB). Horizontal axis is the distance from the ring. Vertical axis is the square root of horizontal and vertical beta functions and the dispersion function [2].	13
2.3	Beam energy, beam current and CDC background in Exp. 61.	13
2.4	CDC and TOF background during Exp. 61. run 1053.	14
2.5	Vertical beam size at the IP(top), beam life time(middle) and CDC current(bottom). horizontal axis of all graphs are time(hour). The run number is 567, the ring is LER, the beam current is 1450 mA, and the mask setting is V-close.	17
2.6	1/life as a function of $1/\sigma_y$ at the IP for the HER (left) and the LER (right). Offset of fitting line is $\tau_{\text{beam-gas}}$	19
2.7	CDC current as a function of beam size at the IP(left) and distribution of CDC current at each beam size(right). Mean of CDC current is the data point. The error of the data point is scaled as so that the $\chi^2 = \text{number of degree}$.	20
2.8	How to estimate $k_{\text{beam-gas}}$ and k_{Touschek} .	20
2.9	CDC current scaled by beam current versus inverse beam life time for HER(left) and LER(right) during beam size scan. The mask setting is V-close.	21
2.10	The fraction of background source(CDC at SuperKEKB).	22
2.11	Wire configuration of the Belle(top) and Belle II(bottom) CDC.	23
2.12	CDC hit rate of Belle CDC	23
2.13	Estimated Belle II CDC hit rate per wire at each layer	24
2.14	SVD hit scaled by beam current versus inverse beam life time for HER (left) and LER (right) during beam size scan. The mask setting is V-close.	24
2.15	The fraction of background source(SVD at SuperKEKB).	25

2.16	The layout of the SVD of Belle (bottom) and SVD/PXD of Belle II (top). Innermost layer of Belle II is replaced by PXD and located smaller radius than Belle.	26
2.17	Design of the TOF/TSC module.	28
2.18	TOF hit rate scaled by beam current versus inverse beam life time for HER (left) and LER (right) during beam size scan. The mask setting is V-close.	28
2.19	The fraction of background source(TOP at SuperKEKB).	29
2.20	ECL energy deposit scaled by beam current versus inverse beam life time for the HER during beam size scan. (a) Whole ECL. (b) Forward region. (c) Backward region. (d) Barrel region.	31
2.21	ECL energy deposit scaled by beam current versus inverse beam life time for the LER during beam size scan. (a) Whole ECL. (b) Forward region. (c) Backward region. (d) Barrel region.	32
2.22	The fraction of background source (ECL at SuperKEKB).	33
3.1	Two possible cooling schemes: one-way (top) and return (bottom).	36
3.2	Pressure drop of paraffin flow through the return cooling beam pipe mockup calculated by Eq.(3.5) as a function of flow rate and Reynolds number. Total flow length is 40 cm. T = 20°C.	40
3.3	Schematic drawing of the cooling test setup.	41
3.4	Measured viscosity and literature value of paraffin.	43
3.5	Pressure drop of paraffin flow through the return cooling beam pipe mockup as a function of flow rate or Reynolds number. Assumed viscosity is the worst pressure drop case, $\nu = 0.002 \text{ Pa*s}$	44
3.6	Schematic drawing of the IP chamber mockup. The symbols A-F describe the position of temperature monitors (PT100). The monitors A and C-F are attached to the mockup surface. The monitor B is inserted in the mockup.	44
3.7	Flow rate is 1 l/min and paraffin temperature is 20 °C. Heater temperature(top), surface temperature(middle), and paraffin temperature(bottom, blue:enter, black:exit).	45
3.8	The surface temperature difference relative to the monitor A. (a) 1 l/min, 20°C (b) 1.8 l/min, 20°C (c) 1.8 l/min, 10°C.	46
3.9	Temperature difference ΔT for each flow rate. Blue and orange points are measured ΔT for 80 W heat source. Green line is the theoretical value calculated by Eq.(3.9) assuming 80 W heat.	47
3.10	Current design of straight part of the beam pipe(top). The one-way cooling scheme is adopted. The mockup of the beam pipe with the one-way cooling system(bottom).	49
4.1	Two SVD designs.	52

4.2	Distribution of expected materials as a function of polar angle(top) and azimuthal angle(bottom) for straight(left) and slant(right) design. SVD sensors, support, electronics, and cooling component are considered [3].	53
4.3	A helical trajectory in x-y plane.	55
4.4	Expected intrinsic resolution in z and phi direction[3].	57
4.5	Resolution of dr (left side) and dz (right side) when polar angle = 90° . Blue line indicate slant and red line indicate straight design. The horizontal axis is the total momentum. Blue line is almost hidden by red line because the difference between slant and straight design is very small.	58
4.6	Resolution of p_t when solenoid magnetic field change. Red lines indicate 1.5T and blue lines indicate 1.2 T. Each marker style indicates the particle momentum (\triangle :0.2 GeV/c, $*$:2.0 GeV/c). The SVD configuration is slant design. The horizontal axis is the polar angle.	59
4.7	Effect of the paraffin gap thickness on tracking parameters. Red lines indicate 1 mm paraffin and blue lines indicate 500 μm . Each marker style indicates the particle momentum (\triangle :0.2 GeV/c, $*$:2.0 GeV/c). The SVD configuration is slant design. The horizontal axis is the polar angle.	60
4.8	Resolution of dr (left side) and dz (right side). The horizontal axis is the polar angle. Blue lines indicate slant and red lines indicate straight design. Each marker style indicates the particle momentum (\bigcirc :0.2 GeV/c, \triangle :0.5 GeV/c, ∇ :1.0 GeV/c, $*$:2.0 GeV/c).	60
4.9	Resolution of dr (left side) and dz (right side) without the PXD. The horizontal axis is the polar angle. Blue line indicate slant and red line indicate straight design. Each marker style indicates the particle momentum (\bigcirc :0.2 GeV/c, \triangle :0.5 GeV/c, ∇ :1.0 GeV/c, $*$:2.0 GeV/c).	61
4.10	Resolution of transverse momentum of SVD+CDC+PXD (left side) and SVD+CDC (right side). The horizontal axis is the polar angle. Blue lines indicate slant and red lines indicate straight design. Each marker style indicates the particle momentum (\bigcirc :0.2 GeV/c, $*$:2.0 GeV/c).	62
5.1	Schematic design of Belle II interaction region.	65
A.1	Movable mask dependence of CDC current per beam current at the LER. Red:both open (Run 574). Blue:vertical masks close, horizontal masks open (Run 567). Green:vertical masks open, horizontal masks close (Run 575). The beam current is 1450 mA, the ring is the LER.	67

A.2	Beam current dependence of CDC current per beam current at the LER. Red:1450 mA (Run 574). Green:1100 mA (Run 577). Blue:750 mA (Run 576). The mask setting is both open.	68
A.3	Bunch number dependence of CDC current per beam current at the LER. Red:bunch number = 1585 (Run 574). Blue:bunch number = 796 (Run 580). The mask setting is both open.	69
B.1	CDC current(top), beam lifetime(middle) and vacuum of the IP(bottom) during IP vacuum bump study of HER(left) and LER(right). The horizontal axis of all graphs are time(hour).	71
B.2	Vacuum pressure at the D1(top), beam life time(middle) and CDC current(bottom) for the HER. The horizontal axes of all graphs are time(hour).	73
B.3	CDC current normalized by beam current versus beam life time for the HER (left) and the LER (right) when vacuum level at upstream of the IR changed.	74
C.1	Hits at around 4×10^5 eV at the 3rd layer of the SVD before (left) and after (right) excluding electric noise. Horizontal axis is the event number. Vertical axis is the number of electron-hole pairs. One electron-hole pair corresponds to 3.6 eV.	76

Chapter 1

Introduction

1.1 Belle-II, the Belle upgrade

The Belle experiment at an asymmetric electron positron collider KEKB finished its operation in June 2010. The Belle experiment accumulated data corresponding to an integrated luminosity of 1000 fb^{-1} . KEKB recorded the world's highest peak luminosity, $2.1 \times 10^{34} \text{ cm}^{-2}\text{s}^{-1}$. The Belle experiment made significant progress including a measurement of large CP violation in the B meson system, which demonstrated that the Kobayashi-Maskawa (KM) mechanism is the dominant source of CP -violation in the standard model. This experimental evidence resulted in the Nobel Prize for physics awarded to M. Kobayashi and T. Maskawa.

The standard model (SM) is a very successful theory in explaining experimental data so far. The SM is, however, not a perfect theory. There are some hints indicating physics beyond the SM. First, the SM has many parameters that are *a priori* unknown. This implies there must be some new, deeper physics beyond the SM. Secondly, the SM cannot account for matter-antimatter asymmetry in the universe. The matter-antimatter asymmetry, CP violation, originating from the KM mechanism is far insufficient to account for the asymmetry. There must be new CP violation mechanism(s) beyond the KM mechanism.

Searches for discrepancy between SM predictions and the measurement provide a good probe for new physics. The flavor changing neutral current (FCNC) processes, such as the radiative decay $b \rightarrow s\gamma$, the semileptonic decay $b \rightarrow sl^+l^-$, and the hadronic decays $b \rightarrow sqq$ or $b \rightarrow dqq$, are sensitive to new physics. It is because FCNC processes are greatly suppressed in the SM via Glashow-Illiopoulos-Maiani (GIM) mechanism and new physics could, if exists, manifest itself in these rare processes.

In order to explore physics beyond the SM using such rare processes, KEKB and Belle will be upgraded to SuperKEKB and Belle II. SuperKEKB will be constructed in the same tunnel that housed KEKB and Belle. Its target lumi-

nosity is ~ 40 times higher than the luminosity achieved by KEKB.

1.2 Luminosity

The production rate of $\Upsilon(4S)$, which simultaneously decays to two B mesons, is calculated by

$$N = \sigma * L, \quad (1.1)$$

where σ is the cross section of the $\Upsilon(4S)$ production of $\sim 10^{-33} \text{ cm}^2$ and L is the luminosity. Because the cross section is constant for each interaction, higher luminosity is required to produce more target particles. Upgrade of SuperKEKB is based on the nano-beam scheme which squeezes a vertical beta function (flat beam) at the interaction point (IP) to improve the luminosity. In this case, the luminosity is described as

$$L = \frac{\gamma_{e^\pm}}{2er_e} \left(1 + \frac{\sigma_y}{\sigma_z}\right) \left(\frac{I_{e^\pm} \xi_y^{e^\pm}}{\beta_y}\right) \left(\frac{R_L}{R_{\xi_y}}\right), \quad (1.2)$$

where γ is the Lorentz factor, r_e is the classical electron radius, $\frac{\sigma_y}{\sigma_z}$ is the ratio of the horizontal and vertical beam size at the IP, I is the beam current, ξ_y is the beam-beam parameter, β_y is the vertical beta function at the IP, and R_L and R_{ξ_y} are the reduction factors for the luminosity and the vertical beam-beam parameter as is defined in [4]. Suffix e^\pm denotes electron(-) or positron(+) beam. $\frac{\sigma_y}{\sigma_z}$ is $<< 1$ (flat beam) and $\frac{R_L}{R_{\xi_y}}$ is ~ 0.8 which is geometrically defined. Thus to increase the luminosity, larger ξ_y , higher beam current, and smaller β_y are required. The vertical beta function near the IP (β_y) can be written as [5]

$$\beta(s) = \beta_{\text{IP}} + \frac{s^2}{\beta_{\text{IP}}}, \quad (1.3)$$

where s is the distance from the IP. This means that the vertical beta function at the IP is limited as

$$\beta_y > d, \quad (1.4)$$

where d is the size of the overlap region. This effect is called hourglass effect.

In the case of the usual head-on collider, $d = \sigma_z$ (bunch length). On the other hand, in the nano-beam scheme with infinite crossing angle, d is determined by

$$d \simeq \frac{\sigma_x}{\phi}, \quad (1.5)$$

where σ_x is the horizontal beam size at the IP and ϕ is the half crossing angle. To shorten the length d , large crossing angle and small horizontal beam size are required. At SuperKEKB, the vertical beta function at the IP is almost 20 times smaller than that of KEKB. For ξ_y , we assume the same value achieved in KEKB. The beam current is twice higher than that of KEKB. With these parameters, SuperKEKB is designed to achieve the luminosity goal of $8 \times 10^{35} \text{ cm}^{-2}\text{s}^{-1}$. Beam parameters of SuperKEKB is shown in Table 1.1.

	KEKB achieved	SuperKEKB
Beam Energy (GeV:HER/LER)	8.0/3.5	7.007/4.000
Beam current(A:HER/LER)	1.188/1.637	2.6/3.6
σ_y at the IP (nm:HER/LER)	940/940	63/48
β_y at the IP (mm:HER/LER)	5.9/5.9	0.30/0.27
σ_x at the IP (μm :HER/LER)	170/147	10/10
β_x at the IP (mm:HER/LER)	1200/1200	25/32
Number of bunch	1584	2500
ξ_y (HER/LER)	0.090/0.129	0.0807/0.0869
Luminosity($10^{34} \text{ cm}^{-2}\text{s}^{-1}$)	2.108	80
Crossing angle (mrad)	22	83

Table 1.1: Beam parameters of KEKB and SuperKEKB. Parameters of KEKB are achieved value [1].

1.3 Belle II detector

The Belle II detector has a total solid-angle coverage of 91% of 4π , which corresponds to the polar angle region from 17° to 150° for trackers and more for the ECL. To achieve higher luminosity, we change the beam size and the beam current which result in higher background. On the other hand, the detector performance is required to be at least as good as that of the Belle detector. Figure 1.1 shows the side view of Belle and Belle II detector and the expected performance of sub-detectors are listed in the Table 1.2. A short description of each sub-detector is given in this section.

1.3.1 SVD/PXD

To accurately measure a vertex position, two silicon pixel detectors (PXD) and four silicon vertex detectors (SVDs) will be introduced. The PXD will be placed closer to the IP (inner $r = 14$ mm) than the innermost layer of the Belle SVD (inner $r = 18$ mm) to achieve better impact parameter resolution. On the other hand, the closer the detector is to the IP, the higher expected background is. Moreover, particles with lower momentum will hit the layers with shorter radii, and therefore can be critical.

To cope with higher background, the updated SVD has a smaller shaping time to reduce occupancy and the PXD has small pixels. The SVD also extends to a larger radius (outer $r = 140$ mm) than Belle (outer $r = 88$ mm) to increase reconstruction efficiency of K_s which decays outside the PXD. There are two designs for outermost SVDs: "slant" and "straight", which is discussed in section 4.1

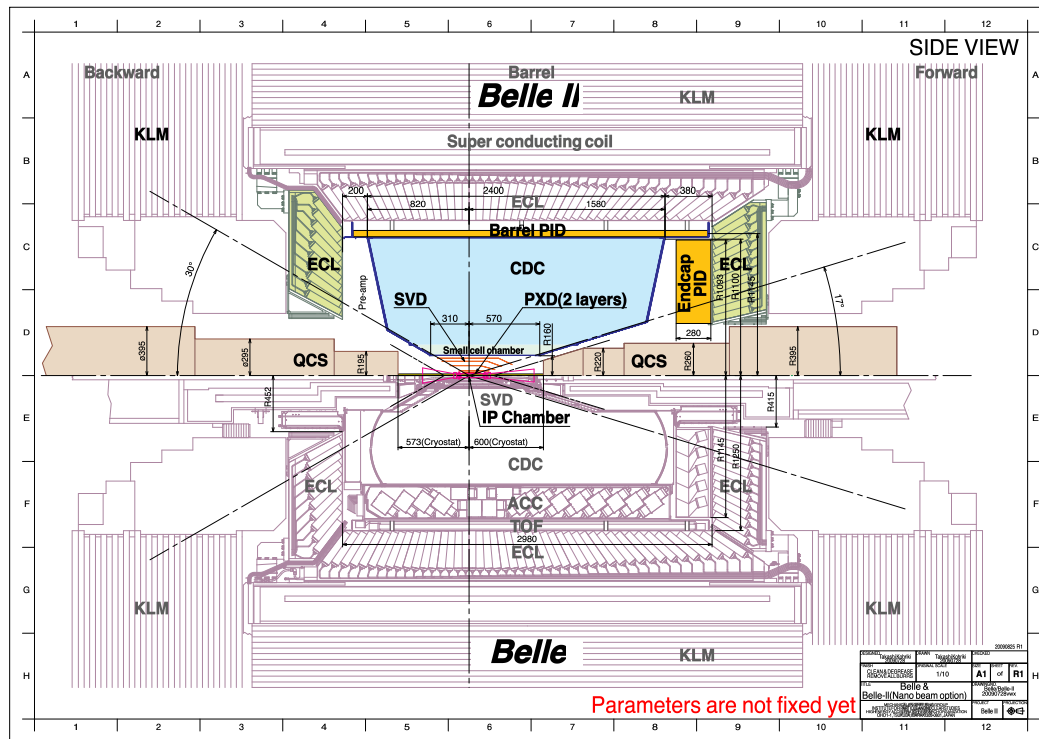


Figure 1.1: Side view of Belle II (top half) and Belle (bottom half) detector for comparison.

Table 1.2: Expected performance of sub-detectors of Belle II.

	Type	Configuration	Performance
PXD	Silicon pixel (DEPFET)	50×50 ($75\text{ }\mu\text{m}$) ² 2 layers: 8 (12) sensors pitch: 50(p)/160(n) - 75(p)/240(n)	impact parameter resolution $\sigma_{z_0} \sim 20\text{ }\mu\text{m}$ (PXD and SVD)
SVD	Double sided Silicon strip	4 layers: 16/30/56/85 sensors μm	
CDC	Small cell drift chamber	56 layers r = 16 - 112 cm $-83 \leq z \leq 159\text{ cm}$	$\sigma_{r\phi} = 100\text{ }\mu\text{m}$, $\sigma_z = 2\text{ mm}$ $\sigma_{p_t}/p_t = \sqrt{(0.2\%\rho p_t)^2 + (0.3\%/\beta)^2}$ $\sigma_{p_t}/p_t = \sqrt{(0.1\%\rho p_t)^2 + (0.3\%/\beta)^2}$ (with SVD) $\sigma_{dE/dx} = 5\%$
TOP	RICH with quartz radiator	16 segments in ϕ at $r \sim 120\text{ cm}$ 275 cm long, 2 cm thick quartz bars with 4x4 channel MCP PMTs	K/ π separation : efficiency > 99% at < 0.5% pion fake prob. for $B \rightarrow \rho\gamma$ decays
ARICH	RICH with aerogel radiator	4 cm thick focusing radiator and HAPD photodetectors for the forward end-cap	K/ π separation at 4 GeV/c: efficiency 96% at 1% pion fake prob.
ECL	CsI(Tl)	Barrel: $r = 125 - 162\text{ cm}$	$\frac{\sigma_E}{E} = \frac{0.2\%}{E} \oplus \frac{1.6\%}{\sqrt{E}} \oplus 1.2\%$
KLM	(Towerized structure) barrel: RPCs	End-cap: $z = -102\text{ cm}$ and +196 cm 14 layers (5 cm Fe + 4 cm gap) 2 RPCs in each gap	$\sigma_{pos} = 0.5\text{ cm}/\sqrt{E}$ (E in GeV) $\Delta\phi = \Delta\theta = 20$ mradian for K_L $\sim 1\%$ hadron fake for muons $\Delta\phi = \Delta\theta = 10$ mradian for K_L $\sigma_p/p = 18\%$ for 1 GeV/ c K_L

1.3.2 CDC

The Central Drift Chamber (CDC) performs three roles. First, it measures charged particle momentum by reconstructing the charged track. Secondly, energy loss within its volume is used for particle identification. Finally, it makes trigger signals for data acquisition.

The basic design of the Belle II CDC is same as the Belle CDC. The same gas mixture He-C₂H₆. To cope with higher background level, drift cells are smaller than Belle. The outer radius extends to where the ACC was located in Belle and the inner radius increases to avoid higher background environment where the SVD will cover instead.

1.3.3 Particle identification(PID)

In Belle II, completely new detectors for K/π identification are used. In the barrel part, TOP counter is used instead of TOF and ACC which were used for Belle. TOP counter measures the time of propagation of the Cherenkov photons. The TOP counter is located in front of the barrel ECL. In the endcap region, Aerogel Ring-Imaging Cherenkov detector (ARICH) is used. The ARICH is located in front of the forward endcap ECL instead of forward endcap ACC which was used for Belle. With these changes, expected K/π identification efficiency is better than that of Belle PID. These changes are also required in order to reduce the material of PID to improve the ECL performance and cope with higher background level.

1.3.4 ECL

The electromagnetic calorimeter (ECL) used in Belle II perform many roles. First, it detects energy and angular coordinates of photons. Secondly, it identifies electrons from other charged particles. Thirdly, it makes trigger signals from energy and cluster information. Finally, it measures luminosity by detecting Bhabha scattering.

Main part of the Belle II ECL is the same as Belle ECL. Its polar angle coverage region is $12.4^\circ < \theta < 155.1^\circ$. CsI(Tl) crystals are used which were also used in Belle ECL. For endcap ECL we planned to use pure CsI crystals. Background can be reduce to $\sim 1/30$ because pure CsI crystals have shorter time constant ($\sim 30\text{ns}$) than CsI(Tl) ($\sim 1\mu\text{s}$). The main issue for pure CsI is the cost. How many or when (1st update or latter) crystals can be replaced depends on the available budget. To cope with higher background levels, the shaping time is changed from $1\ \mu\text{s}$ to $0.5\ \mu\text{s}$ and wave-form sampling is adopted.

1.3.5 K_L^0 and μ detector (KLM)

KLM, the outermost detector of Belle II, is for detecting K_L and identifying μ . KLM consists of an alternating sandwich of iron plates and Resistive Plate Chamber(RPC) for barrel KLM or scintillator-based detector for endcap KLM.

Hadrons make hadronic shower through iron plates and deposit their energy. μ s don't make shower and penetrate KLM. Extrapolating the charged track which is reconstructed using the SVD and the CDC, μ s are identifiable. Neutral particles K_L^0 s are identifiable from KLM signal with no signal from other detectors. Its polar angle coverage region is $20^\circ < \theta < 155^\circ$.

1.4 Interaction Region(IR) issues

The interaction region (IR) is the connection region between the Belle II detector and the SuperKEKB accelerator. It contains the beam pipe and the SVD/PXD. To achieve high luminosity with the nano-beam scheme, we have to design a new interaction region for Belle II. Figure 1.2 shows the interaction region of Belle and Belle II. There are more components in the IR. For example, the PXD is introduced at the innermost of the detector. The crotch part of the beam pipe is located within the IR and final focusing magnets are also located closer to the IP due to a larger crossing angle. Because of these changes less space is available for the IR. It is also important to decrease background particles. For example, the beam pipe is designed to avoid direct synchrotron radiation hits.

To design this new interaction region, we need to solve several problems shown in following paragraph. In this thesis, we show the discussion for solving those problems.

First of all, beam-induced background is expected to increase with higher luminosity, especially Touschek backgrounds increase steeply because of much smaller beam size. From rough estimation by machine parameter scaling, it was estimated that the beam background is 20 times higher than Belle. To estimate more precisely, a beam test study is conducted. The beam test study for estimating Touschek and beam-gas background at SuperKEKB is discussed in chapter 2. Touschek and beam-gas background are also studied by simulation based on TURTLE and GEANT3. To check the validity of simulation, we measured SVD occupancy with Belle data and compare it with simulation results for Belle(Appendix C). The simulation study for Belle II is ongoing. Other background, such as synchrotron radiation, QED background are also being studied.

The manifold for the beam pipe cooling system which is used in Belle can conflict with the PXD read out chips or cables for readout. We have to pursue the possibility of a "return cooling system". We discuss cooling capability of the return cooling system in chapter 3. We are now also thinking about a "one-way" cooling system. Its cooling capability is also discussed in chapter 3. We also discuss selection of the coolant.

To reduce these higher background particles hitting at the SVD and the PXD, we put the heavy metal shield near the IR. The design of the heavy metal shield depends on the layout of the outer layer of the SVD: "slant" or "straight". To choose the layout of the SVD, we have to understand the difference of performance between both designs. We perform simulation study to understand the difference in resolution of impact parameters which is discussed in chapter 4.

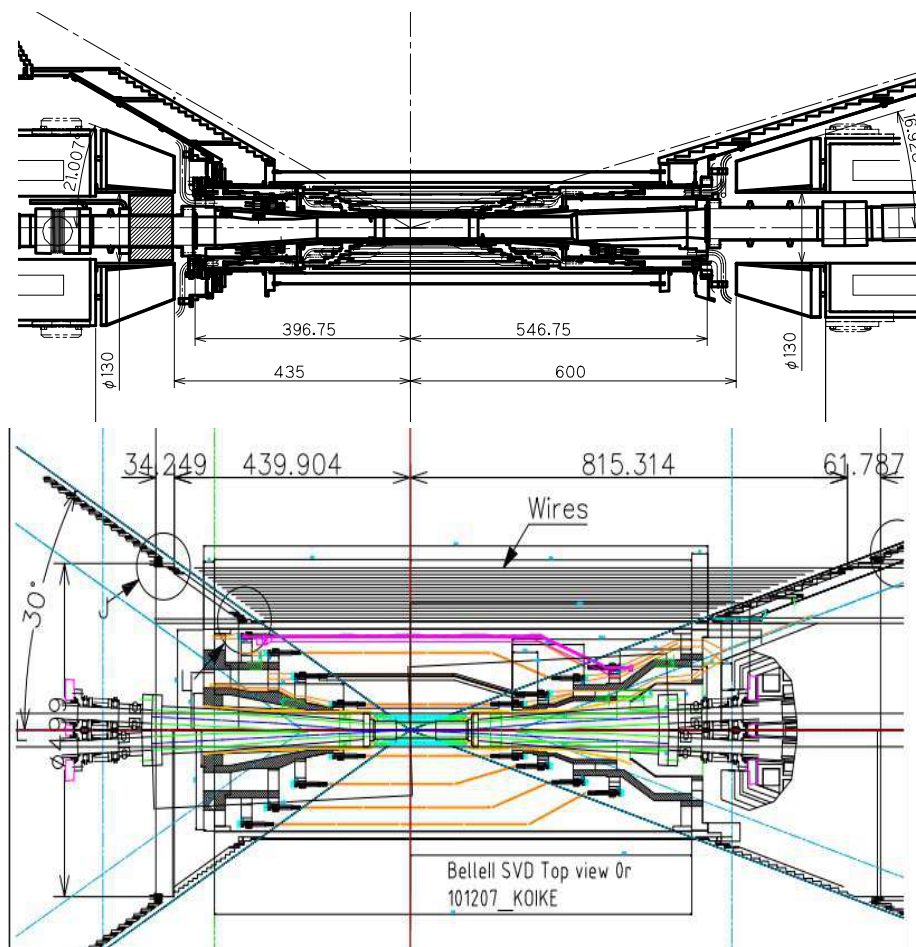


Figure 1.2: Schematic layout of the interaction region of Belle (top) and Belle II (bottom).

Chapter 2

Estimation of beam background of SuperKEKB

In this chapter we present the beam test study and analysis for estimating beam background level at SuperKEKB.

2.1 Main background sources at SuperKEKB

In SuperKEKB, the luminosity will be improved by squeezing the beta function at the IP, and by increasing the number of bunches and beam currents. These changes will in turn cause an increase of the beam-induced background.

There are seven major types of beam-induced background sources at SuperKEKB: Beam-gas scattering, Touschek scattering, synchrotron radiation(SR) from the high energy ring(HER) upstream direction, backscattering of SR from HER downstream, radiative Bhabha scattering, electron-positron pair production via two photon processes, and beam-beam background.

- Beam-gas

Beam-gas scattering is coulomb scattering and bremsstrahlung due to electron or positron interaction with residual gas. Particles change direction due to Coulomb scattering or lose energy from bremsstrahlung. Particles which deviate a lot from their original path directly hit the detector or hit vacuum chambers and magnets and generate particle showers. These secondary particles hit the detector as background particles. Coulomb scattering can be reduced by both vertical and horizontal movable masks and bremsstrahlung can be reduced by inside horizontal masks.

This scattering rate is proportional to the beam current and the vacuum pressure. In SuperKEKB, beam current of the LER and HER increase from 1.6 A to 3.6 A and 1.2 A to 2.6 A respectively. The vacuum level of SuperKEKB will be the same as the current KEKB except for the

IR region. The average vacuum level of KEKB is $\sim 10^{-8}$ Pa. The vacuum level of the IP, however, will be 100 to 1000 times worse than the current value. The effect of this degraded vacuum at the IP is studied (See Appendix B). From this study, degraded vacuum level at the IP region causes more beam loss but background to the detector found to be unchanged. Thus the beam-gas background increase about twice.

- Touschek effect

Touschek effect is an intra-bunch scattering. Coulomb scattering between two particles in the beam bunch changes their energy to deviate from beam bunch, one with too much and the other with too little energy. These scattered particles also hit the beam pipe and make showers. The scattering rate of the Touschek effect is proportional to the inverse beam size, third power of the beam energy, the number of bunch and second power of the bunch current. Background from the Touschek effect will become much higher at SuperKEKB due to the smaller beam size. The contribution from the LER is much higher than the HER because of asymmetric beam energy. As shown in Table 1.1, we change the beam energy from $(E_{\text{HER}}, E_{\text{LER}}) = (8.5 \text{ GeV}, 3.5 \text{ GeV})$ to $(E_{\text{HER}}, E_{\text{LER}}) = (7.0 \text{ GeV}, 4.0 \text{ GeV})$. One reason that we change beam energy to be less asymmetric is to reduce the Touschek effect from the LER.

With beam parameters shown in Table 1.1 and averaged beta functions at whole ring [6], the scattering rate of Touschek effect is expected to increase ~ 18 times and ~ 24 times for LER and HER respectively from simple estimation by machine parameter scaling.

Background by Touschek effect can be reduced by both inside and outside horizontal movable masks because scattering particles have too much or little energy. KEKB has, however, only inside movable masks. In SuperKEKB, outside movable masks will be introduced and the Touschek background will be reduced.

- SR from upstream

It is important to evaluate SR background to protect SVD/PXD. Since the SR power is proportional to the beam energy squared and magnetic field squared, the HER beam is the main source of this type of background. The energy of SR is few keV to tens of keV. At the first stage of Belle, the inner layer SVD was severely damaged by x-rays with $E \sim 2\text{keV}$ from HER. To reduce the synchrotron radiation background, we coated the inner surface of the beam pipe with gold plate. In Belle II, inner surface of the beryllium pipe is also plated by gold in order to reduce synchrotron radiation. The IR beam pipe is designed to avoid direct SR hits at the detector. SR also depends on magnet position, bending radii and beam orbit. Careful simulation is studied by the background simulation group.

- Backscattering of SR from downstream

In KEKB, the final focusing magnet, called QCS, acts as not only as the final focusing magnet of the LER beam but also as the bending magnet of HER beam. Strong SR is emitted because of this bending magnet. On the other hand, at SuperKEKB, final focusing magnet will be separated and both incoming and outgoing beams are on centered in the magnet. We therefore expect much lower background than KEKB.

- Radiative Bhabha scattering

The rate of radiative Bhabha scattering is proportional to the luminosity. Photons from this scattering propagate along the beam direction and hit at the magnet. In this interaction, many neutrons are produced which become main background source for the KLM.

- Electron-positron production via two-photon process

We have to consider the very low momentum electron-positron pair background because the PXD will be located closer to the IP (beam pipe radius will be only 10mm). The occupancy of the PXD resulting from these particles will be 0.1 to 1.5% when pixel number of the first layer is 3.2M and integration time is 20 μ s. Bhabha scattering and two-photon process are collectively called the QED background.

- Beam-beam interaction

A beam bunch interacts with the electric field of the other bunch when they collide at the IP. A beam particle is kicked by this interaction and can be the background source. This kick force is almost proportional to the distance from the center of the bunch at $x/\sigma \ll 1$. [5][7]. Actually, it is difficult for study this interaction precisely because the interaction is a non-linear force and we have not understood well the effect of this interaction on detector background. A simulation study to estimate the background level of beam-beam interaction will be performed.

To summarize, the Touschek effect can be the largest background source because the beam size will be squeezed to 1/20 and Touschek scattering will be extremely higher than KEKB. The Touschek effect, however, is not understood well in the Belle experiment. It is important to estimate the distribution of the Touschek effect. We estimate the background of Touschek and beam-gas effects from the beam test study.

2.2 Masks

To reduce background, a mask system will be introduced. There are two types of mask systems, fixed and movable.

The fixed masks are located near the Belle detector in order to fill the unshielded area against particle showers generated by off momentum particles hitting the beam pipe and direct hits from off momentum particles. These masks

are composed of Tungsten. When the mask thickness is few radiation lengths, a particle hitting the mask generates showers resulting in background. We should fill empty space with heavy metal as much as possible. A heavy mask, however, it is difficult to support. We have to optimize the position and the amount of heavy metal to shield beam background particles effectively.

The movable masks are located near the arc section of the beam line (Figure 2.1). The movable mask should be located where the beta function and the dispersion function is large so that the movable mask can act as a collimator (Figure 2.2). In KEKB, two vertical masks (up, down) and two horizontal masks (both inside) were set in each region. There are no outside horizontal masks in Belle. In Belle II, however, Touschek background will be expected to be larger than Belle. Outside masks can be useful for reducing Touschek background because beam loss from Touschek can involve large energies. We introduce both inside and outside horizontal masks. The location of the mask system will be optimized for the optics of SuperKEKB so that beam background can be reduced effectively.

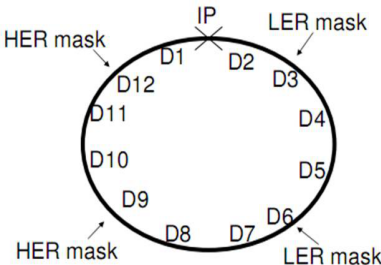


Figure 2.1: The location of movable masks in the KEKB ring.

2.3 Typical run of KEKB

To compare the estimated SuperKEKB background with current KEKB one, we choose a run with nominal beam condition and define it as a "typical" run.

Figure 2.3 shows the beam environment and CDC background during Exp.61, the operation at the energy of the $\Upsilon(4S)$ resonance. Exp.61 Run1053 data set is selected as the typical KEKB run because it has enough data and beam seems to be stable during this run. SVD hits per trigger, current of HV supplied for the CDC inner three layers, ECL total energy deposit, TOF trigger rate are measured in this run. Table 2.1 shows the parameters at this run and Figure 2.4 shows the CDC and the TOF background during this run. In this run, the average CDC current is $13 \mu\text{A}$, SVD hit is 150 hits/trigger ($>10 \text{ keV}$), ECL energy deposit ($> 1 \text{ MeV}$) is 7.1 GeV, and TOF hit rate is about 90 kHz.

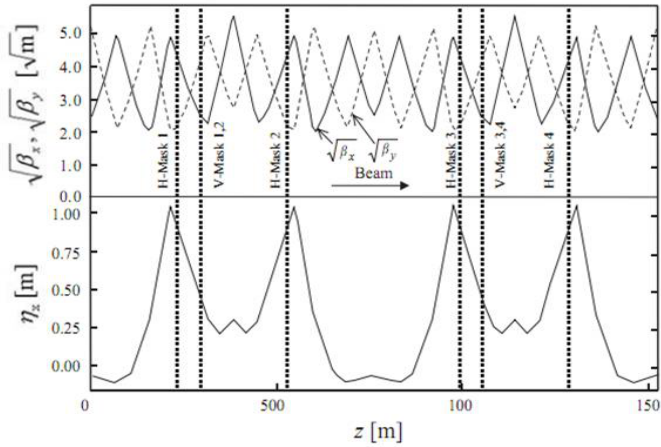


Figure 2.2: The location of movable masks in the beam lattice diagram (LER of KEKB). Horizontal axis is the distance from the ring. Vertical axis is the square root of horizontal and vertical beta functions and the dispersion function [2].

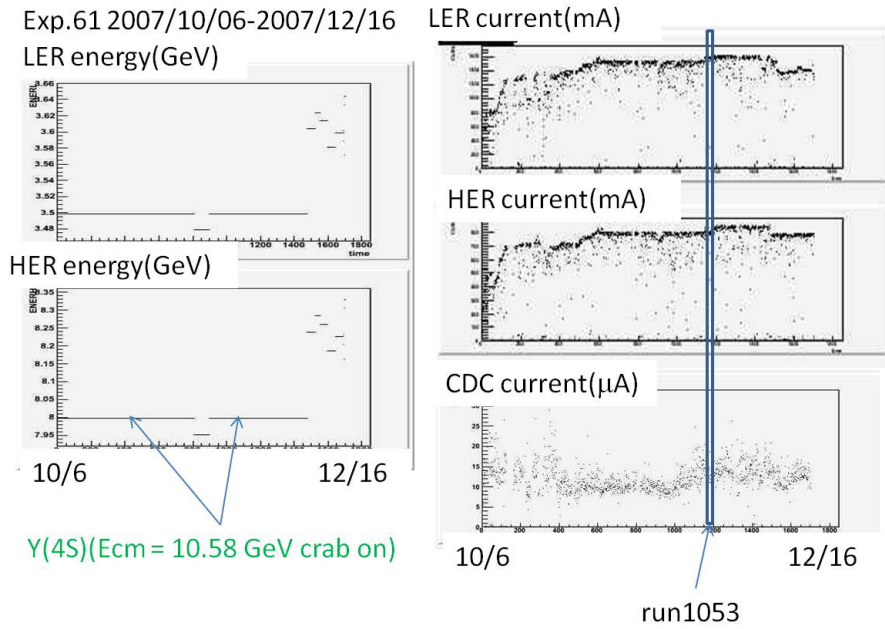


Figure 2.3: Beam energy, beam current and CDC background in Exp. 61.

	HER	LER
Energy(GeV)	7.997	3.4998
Beam current(A)	0.822	1.590
Life time(min)	154	152
Vertical beam size(μm)	2.2	2.5
Average vacuum(Pa)	2.2E-8	6.5E-8
Peak luminosity($\text{cm}^{-2} \text{ s}^{-1}$)	144.73E32	

Table 2.1: Machine parameters of Exp.61 run1053.

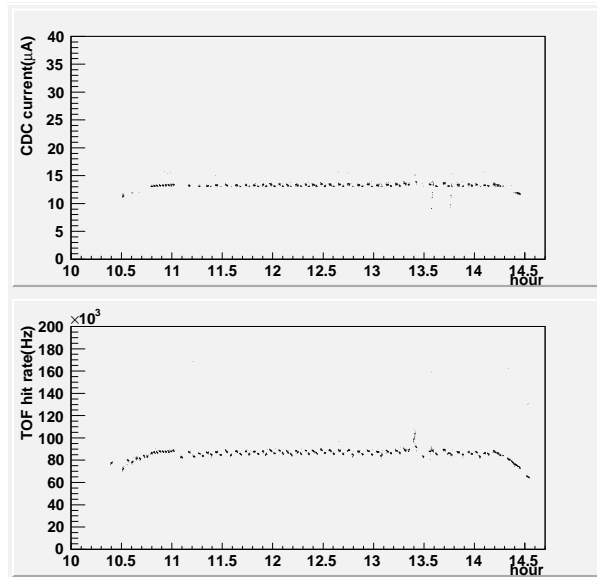


Figure 2.4: CDC and TOF background during Exp. 61. run 1053.

2.4 Touschek study

A beam test called "Touschek study" was performed on June 7th and 8th at KEKB. In this study, the vertical beam size is scanned in order to separate the contribution from the Touschek effect and other backgrounds. The background of each sub-detector, SVD, CDC, TOF, and ECL are checked.

2.4.1 Settings

The the conditions of Touschek study are summarized in Table 2.2. We scanned the vertical beam size in each run. We can separate background of Touschek effect and other background by studying the beam size dependence because only Touschek background depends on the beam size. The Vertical beam size is changed by changing i-size-bump which is the offset of the beam from the center of the sextupole magnet after the bending magnet. Beam emittance is changed by i-size-bump which result in changing the vertical beam size at whole ring[8].

Run No. (Exp.73)	Description	Mask setting	Beam current (mA)	Ring
564	beam current dependence($1 \mu\text{m}$)	both open	-	LER
567	size sweep	V-close	1450	LER
574	size sweep	both open	1450	LER
575	size sweep	H-close	1450	LER
576	size sweep(smaller current)	both open	750	LER
577	size sweep(smaller current)	both open	1100	LER
580	half number of bunch(796)	both open	725	LER
594	size sweep	both open	850	HER
595	size sweep	V-close	850	HER
596	size sweep	H-close	850	HER
597	size sweep(smaller current)	both open	400	HER
598	size sweep(smaller current)	both open	600	HER

Table 2.2: Summary of Touschek study. V-close means vertical masks are closed and horizontal masks are open. H-close means vertical masks are opened and horizontal masks are closed. Both open means both vertical and horizontal masks are opened.

At first, we check how small or large we can change the beam size and we fix the beam size range as $1.2 \mu\text{m}$ to $4 \mu\text{m}$. Second, movable mask condition is defined. The "mask close" setting corresponds to normal physical setting. The "mask open" setting corresponds to the one when we open masks as much as we can. We open the mask gradually from physics setting to check how much masks can be opened because if background level is too high Belle cannot operate. It is found that all horizontal masks but D12H4 can be opened up to 20 mm. The position of the D12H4 mask is 19 mm, almost opened, for both close and

open setting because the background somehow increased as the D12H4 mask closed. Almost all Vertical masks can be opened 1 mm wider than in physics run setting, while D03V4 mask can be opened during just physics run setting plus 0.5 mm because of high background levels. Beam current is constrained to change within 5% and horizontal beam size is also constrained to change within 2%. After finishing these checks, we finally commence a single beam run. Under these conditions, background levels of each detector are measured, CDC current of innermost three layers, TOF hit rates are given from Uehara database and SVD hits per trigger and total energy deposit per trigger to ECL are obtained from raw data taken by random trigger.

Figure 2.5 shows the typical run for Touschek study, Run 567. The data contaminated by beam injection period is excluded by the condition of beam life time being 0(no data). We find smaller life time and more background ascribed to more Touschek effect caused by smaller beam size.

2.4.2 Background estimation strategy

To estimate the background level at SuperKEKB, we use

$$\text{Background} = I \cdot \left(k_{\text{Touschek}} \cdot \frac{1}{\tau_{\text{Touschek}}} + k_{\text{beam-gas}} \cdot \frac{1}{\tau_{\text{beam-gas}}} + \dots \right), \quad (2.1)$$

where τ is the beam life time due to the beam loss of each background source and I is the beam current, assuming that background should be proportional to beam loss. The proportional constant k indicates the effect on the detector from beam loss at whole ring which are different for each sub-detector. The proportional constant k also depends on movable mask setting or fixed type masks. Thus, we have to know k and τ of SuperKEKB for each background source and for each sub-detector.

In Eq.(2.1), τ can be dependent on bunch current. The cross section of Touschek is related to two particles in the beam bunch, thus $\frac{dI}{dt}_{\text{Touschek}} \propto I_{\text{bunch}}^2$. The cross section of the beam-gas is related to one particle in a bunch and a surrounding particle, thus $\frac{dI}{dt}_{\text{beam-gas}} \propto I_{\text{bunch}}$. These simple estimations and definition of life time $1/\tau = \frac{1}{I} \frac{dI}{dt}$ yield the relation

$$\frac{1}{\tau_{\text{Touschek}}} \propto I_{\text{bunch}} \quad (2.2)$$

$$\frac{1}{\tau_{\text{beam-gas}}} = \text{Const}, \quad (2.3)$$

or

$$\text{Background}_{\text{Touschek}} \propto N_{\text{bunch}} \cdot I_{\text{bunch}}^2 \quad (2.4)$$

$$\text{Background}_{\text{beam-gas}} \propto N_{\text{bunch}} \cdot I_{\text{bunch}}. \quad (2.5)$$

To confirm the current dependence of background, beam current dependence (section A.2) and number of bunch dependence (section A.3) are checked. To

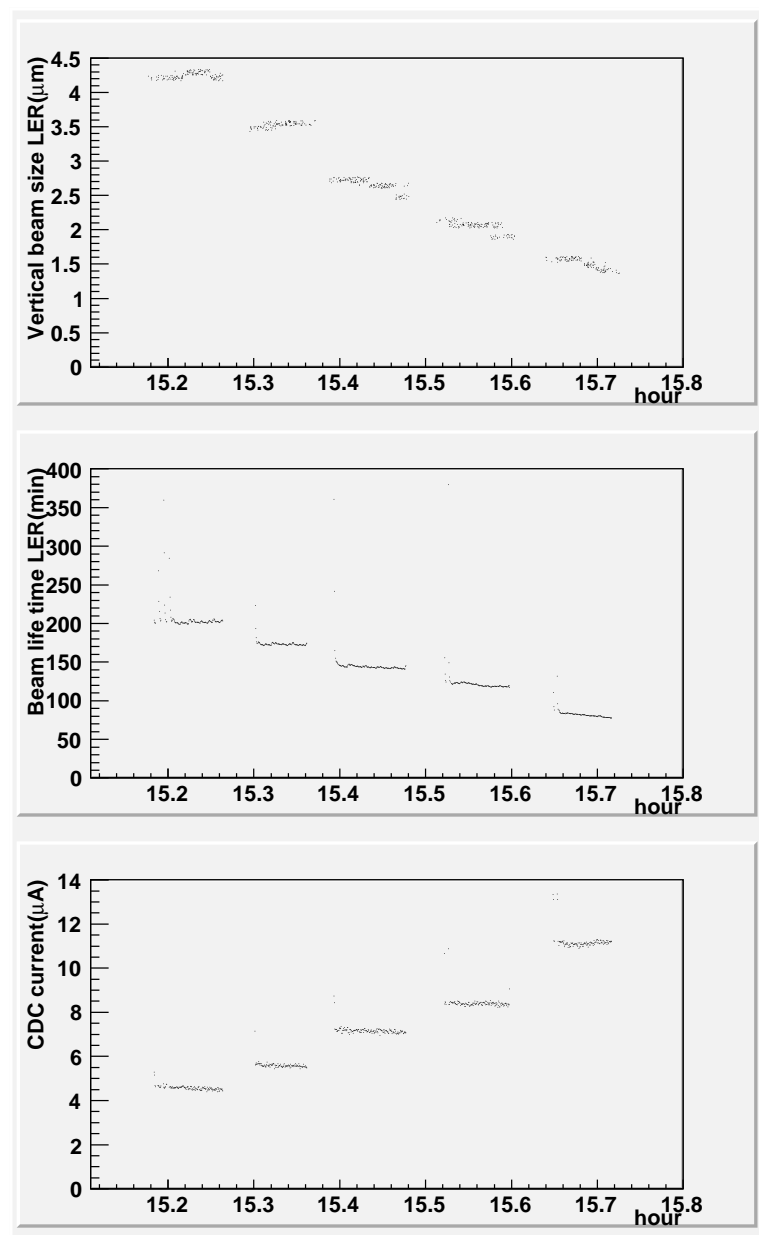


Figure 2.5: Vertical beam size at the IP (top), beam life time (middle) and CDC current (bottom). horizontal axis of all graphs are time (hour). The run number is 567, the ring is LER, the beam current is 1450 mA, and the mask setting is V-close.

avoid this current dependence, we operate the beam test under constant current condition. The Vertical mask close condition is used for the estimation because we want to estimate background under the same condition as physics run setting.

The overall strategy of background estimation is as follows.

1. Measure $\tau_{\text{beam-gas}}$ (section 2.5.1), k_{Touschek} and $k_{\text{beam-gas}}$ for each detector (section 2.5.3-2.5.6) at KEKB by machine study.
2. $\tau_{\text{beam-gas}}$ at SuperKEKB is assumed to be same as KEKB because the vacuum level at SuperKEKB is assumed to be at similar level except for the IP region. The vacuum level near the IP at SuperKEKB is expected to be worse than KEKB. The beam loss due to degraded vacuum at the IP, however, doesn't effect on the detector background. We can assume that the beam loss (life time) by beam-gas scattering which causes detector background is at similar level as KEKB. The k_{Touschek} and $k_{\text{beam-gas}}$ at SuperKEKB are also assumed to be the same as KEKB. Thus, we use the measured value for our extrapolation.
3. The life time of the Touschek effect at SuperKEKB, difficult to predict from beam test because of drastic change of beam optics, is calculated by optics simulation using SAD, a simulation program for accelerator design, $\tau_{\text{Touschek}}^{\text{LER}} = 10 \text{ min}$ and $\tau_{\text{Touschek}}^{\text{HER}} = 10 \text{ min}$ [9].
4. Assume that the beam background of sub-detectors is dominated by Touschek and beam-gas scattering. The value we call "beam-gas" is actually the value for "no-Touschek effect" and may include not only beam-gas background but also other background such as SR. We don't have to consider beam-beam interaction and Bhabha scattering because we operate a single beam run. We assume conservative case that there is no SR background. We have to estimate SR background in another way.
5. So far, we know all parameters to calculate the background level at SuperKEKB assuming that current Belle detector is used for SuperKEKB (section 2.5). After the extrapolation, we check if the Belle II detector is tolerable to beam background by comparing with current Belle detector.

2.5 Estimation of background level of each detector

In this section, we evaluate $\tau_{\text{beam-gas}}$, k_{Touschek} and $k_{\text{beam-gas}}$ which are defined in section 2.4.2 and estimate the background of each sub-detector.

2.5.1 Estimation of $\tau_{\text{beam-gas}}$

At first, we estimate $\tau_{\text{beam-gas}}$ at the current KEKB. Figure 2.6 shows the vertical beam size dependence of inverse life time at the LER and the HER which is fitted well by linear function because the beam loss by the Touschek

effect is proportional to the beam size. Figure 2.7 shows how to define data point and the error bar in figure 2.6. Each data points are the mean value at the same beam size. The error of each point is at first calculated as the RMS/ $\sqrt{\text{entries}}$, and then it is scaled so that the reduced χ^2 become unity of the fit. The same method is used for other analysis in following sections.

When the beam size is too large, the Touschek effect is negligible. The offset of fitting line is the beam loss by non-Touschek scattering, which is assumed to contain only beam-gas effect($1/\tau_{\text{beam-gas}}$). Increase from this offset at nominal beam size is the beam loss by the Touschek effect($1/\tau_{\text{Touschek}}$) because the ratio of beam-gas scattering or other background is independent of the beam size. From Figure 2.6, $\tau_{\text{beam-gas}}^{\text{HER}} = 3400 \pm 3500$ min, $\tau_{\text{beam-gas}}^{\text{LER}} = 800 \pm 120$ min. The life time of Touschek effect at KEKB is also obtained at arbitrary beam size. When the vertical beam size is $2 \mu\text{m}$, $\tau_{\text{Touschek}}^{\text{HER}} = 1300 \pm 500$ min, $\tau_{\text{Touschek}}^{\text{LER}} = 130 \pm 4$ min. The beam loss by Touschek scattering is studied by H Nakano in his KEKB accelerator simulation study. In his study, τ_{Touschek} is calculated to be 1790 min and 109 min for HER and LER respectively. It is found that our measured Touschek life time is consistent with the simulation results.

Though this is the life time of KEKB, we use the same beam-gas life time for SuperKEKB background estimation because we assume that SuperKEKB will achieve same vacuum level(same beam loss at whole ring).

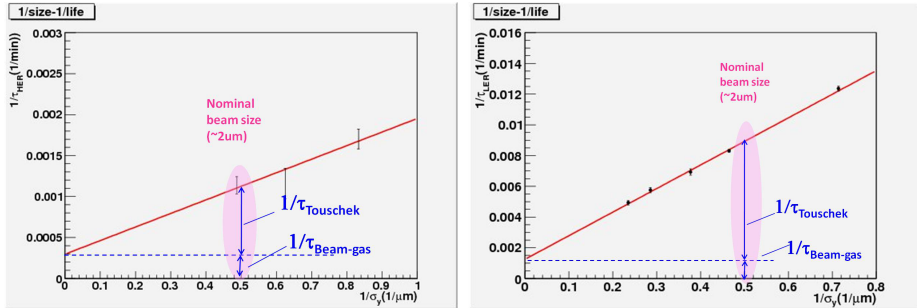


Figure 2.6: $1/\text{life}$ as a function of $1/\sigma_y$ at the IP for the HER (left) and the LER (right). Offset of fitting line is $\tau_{\text{beam-gas}}$

2.5.2 Estimation of $k_{\text{beam-gas}}$ and k_{Touschek}

Figure 2.8 shows how to estimate $k_{\text{beam-gas}}$ and k_{Touschek} for each sub-detector. At first, the relation between the background per the beam current and the inverse life time is fitted linearly (1). Because only the vertical beam size is changed during the study, the slope of red line is the k_{Touschek} . Next, fitted function should be extrapolated to $1/\tau_{\text{beam-gas}}$ which is known in section 2.5.1 (2). Finally, we extend the green line to the origin of the graph (3). The slope of this green line is the $k_{\text{beam-gas}}$. This type of graph can be drawn for each sub-detector and $k_{\text{beam-gas}}$ and k_{Touschek} for each detector are obtained in following

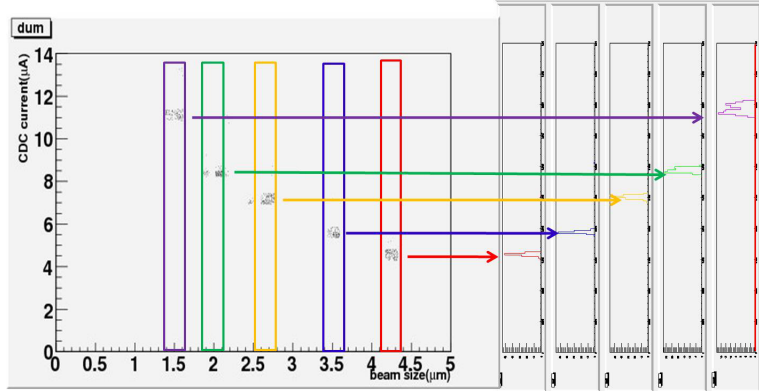


Figure 2.7: CDC current as a function of beam size at the IP(left) and distribution of CDC current at each beam size(right). Mean of CDC current is the data point. The error of the data point is scaled as so that the $\chi^2 = \text{number of degree}$.

section.

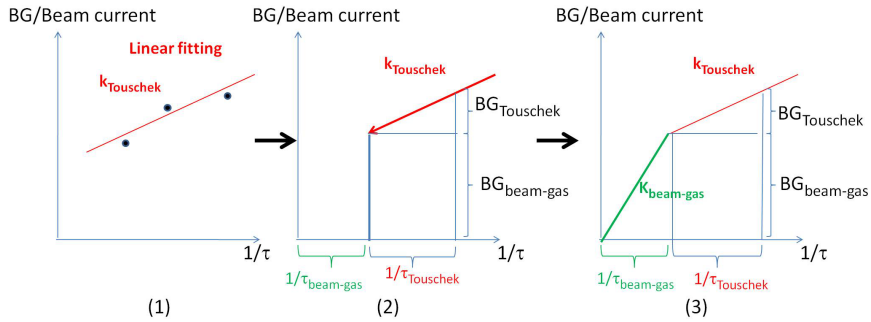


Figure 2.8: How to estimate $k_{\text{beam-gas}}$ and k_{Touschek} .

2.5.3 CDC

CDC current of innermost three layers is used for the estimation of the CDC background. Figure 2.9 shows the CDC current scaled by beam current as a function of the beam life time. The plot is fitted well by a linear function. From this graph, we can evaluate both k_{Touschek} and $k_{\text{beam-gas}}$ as is shown in section 2.5.2.

Now we know all parameters to calculate the background of the CDC at SuperKEKB. Table 2.3 shows the each parameters and estimated background

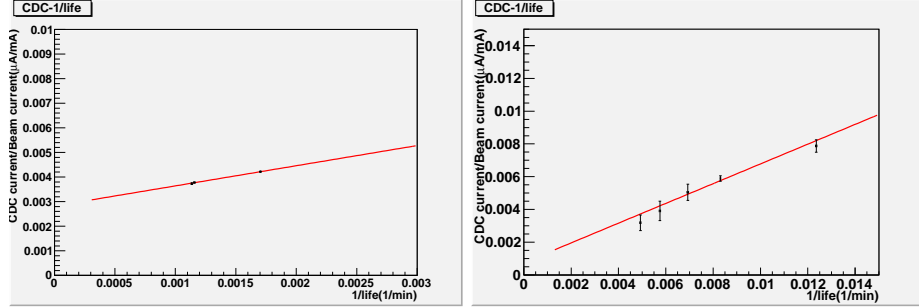


Figure 2.9: CDC current scaled by beam current versus inverse beam life time for HER(left) and LER(right) during beam size scan. The mask setting is V-close.

	$k_{\text{beam-gas}}$ ($\mu\text{A}\cdot\text{min}/\text{mA}$)	k_{Touschek} ($\mu\text{A}\cdot\text{min}/\text{mA}$)	CDC current (μA)
HER	10 ± 9	0.82 ± 0.03	220 ± 10
LER	1.2 ± 0.5	0.60 ± 0.07	220 ± 30
total	-	-	440 ± 30

Table 2.3: $k_{\text{beam-gas}}$ and k_{Touschek} for CDC current and expected CDC current if we put the same CDC at the same place as Belle under the conditions of SuperKEKB.

level if we use the Belle CDC at the same place under the SuperKEKB conditions. Figure 2.10 is the pie graph of estimated background fraction. The main background source is the Touschek effect, $\sim 97\%$.

To consider the effect of this expected background on the Belle II CDC we translate CDC current into CDC hit rate. The wire configuration of Belle II CDC is shown in Table 2.4 and Figure 2.11. The acceptance region is the same as the Belle CDC. To reduce occupancy, the Belle II CDC has more cells in each layer than the Belle CDC layer at the same radius and the radius of the innermost layer increases. Background effect on the Belle II CDC is estimated by extrapolating from CDC hit rate at KEKB. The hit rate per wire at each layer of the Belle CDC is known in Exp.41, run 1128 (Figure 2.12[10]). In this run, CDC current is $\sim 21 \mu\text{A}$. CDC hit rate at SuperKEKB is estimated by simply extrapolating at the same rate of CDC current from Belle CDC hit rate of the layer placed at the same radius and multiply scale factor by the cell number as is shown in

$$(\text{hit rate})_{\text{Belle-II}} = (\text{hit rate})_{\text{Belle}} \cdot \frac{(\text{CDC current})_{\text{Belle-II}}}{(\text{CDC current})_{\text{Belle}}} \cdot \frac{(\#\text{Cell})_{\text{Belle}}}{(\#\text{Cell})_{\text{Belle-II}}}. \quad (2.6)$$

Figure 2.13 shows the estimated CDC hit rate of Belle II. The estimated

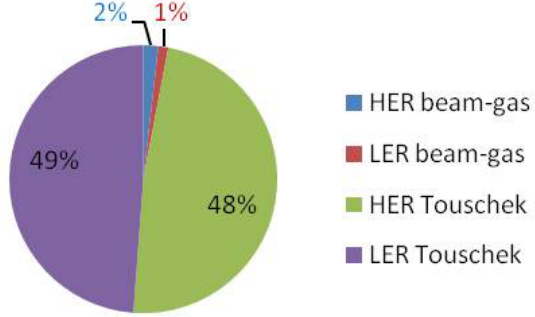


Figure 2.10: The fraction of background source(CDC at SuperKEKB).

hit rate of the Belle II CDC is 84 kHz at layer 6 which corresponds to the innermost super layer of the Belle II CDC or less at outer main layers. The innermost layer of the Belle CDC can operate under the condition of around 200 kHz hit rate [11]. The estimated background is less than that of innermost layer of Belle CDC, and it is concluded that the CDC works under expected background level.

Super layer type and No.	No. of layers	Signal cells per layer	radius (mm)
Axial 1	8	160	168.0-238.0
Stereo U2	6	160	257.0-348.0
Axial 3	6	192	365.2-455.7
Stereo V4	6	224	476.9-566.9
Axial 5	6	256	584.1-674.1
Stereo U6	6	288	695.3-785.3
Axial 7	6	320	257.0-348.0
Stereo V8	6	352	913.7-1003.7
Axial 9	6	384	1020.9-1111.4

Table 2.4: Configuration of the Belle II CDC sensor wires.

2.5.4 SVD/PXD

SVD hits per trigger is used for the estimation of the SVD background. Random trigger data set during the Touschek study is used for this analysis.

SVD readout system sets the threshold as 3 times of the noise level which is ~ 3000 electron-hole pairs, one electron-hole pair corresponds to 3.6 eV, when

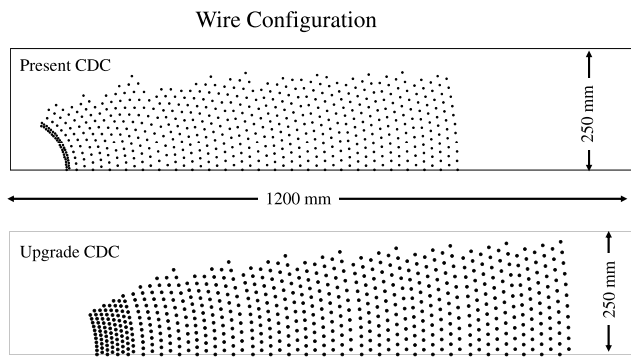


Figure 2.11: Wire configuration of the Belle (top) and Belle II (bottom) CDC.

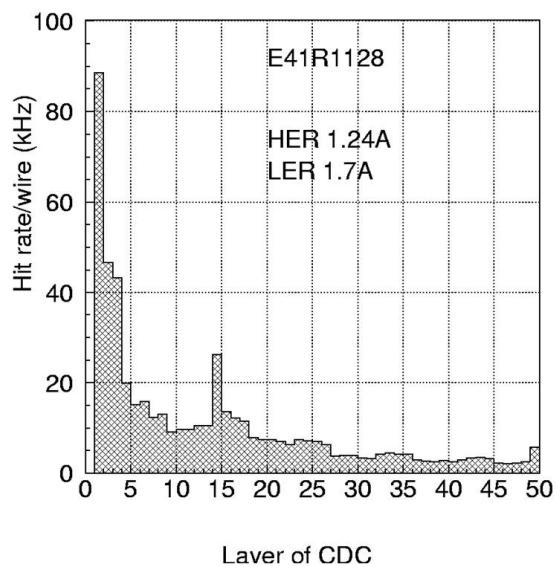


Figure 2.12: CDC hit rate of Belle CDC

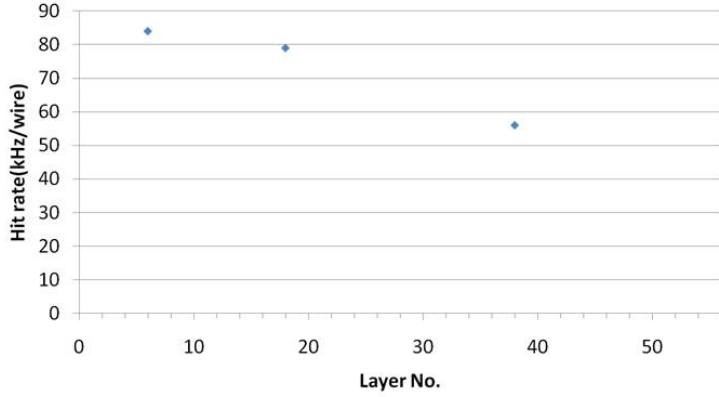


Figure 2.13: Estimated Belle II CDC hit rate per wire at each layer

S/N ratio is 20. When one strip is over the threshold voltage, however, neighboring strips are read out at the same time. So, there are many hits with energy less than 10 keV. We analyze both the data with this low energy hit data and the data from which low energy hits are excluded.

At first, the data with low energy hit is analyzed and background of the SVD 1st layer at SuperKEKB is estimated. The relation between SVD hit per trigger scaled by beam current and the inverse life time is shown in Figure 2.14. The $k_{\text{beam-gas}}$ and k_{Touschek} are obtained based on this information. Each parameter and estimated background if we use the Belle SVD at the same place, radius = 1.5 cm, under the SuperKEKB conditions are shown in Table 2.5. Figure 2.15 is the pie graph of estimated background fraction. The main background source is the Touschek effect, $\sim 95\%$.

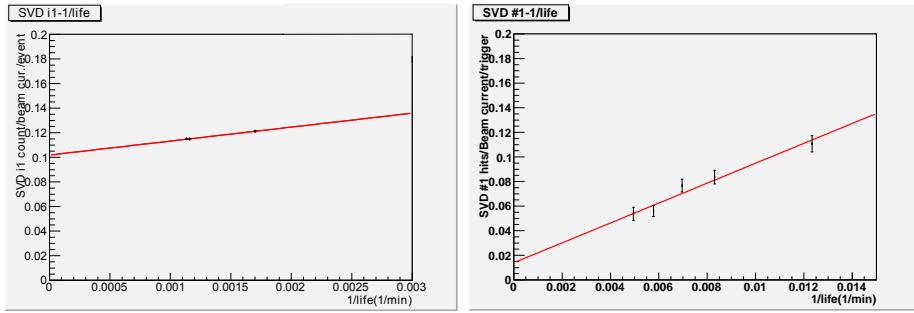


Figure 2.14: SVD hit scaled by beam current versus inverse beam life time for HER (left) and LER (right) during beam size scan. The mask setting is V-close.

To consider the effect of this expected background on the Belle II SVD, we translate SVD hit per trigger into SVD occupancy. Figure 2.16 shows the

	$k_{\text{beam-gas}}$ (hits·min/mA)	k_{Touschek} (hits·min/mA)	hits at SVD 1st layer (hits/trigger)
HER	360 ± 360	11.4 ± 0.8	3200 ± 400
LER	16 ± 19	9 ± 1	3300 ± 400
total	-	-	6500 ± 600

Table 2.5: $k_{\text{beam-gas}}$ and k_{Touschek} for SVD hit and expected SVD hit if we put the same SVD at the same place as Belle under the conditions of SuperKEKB.

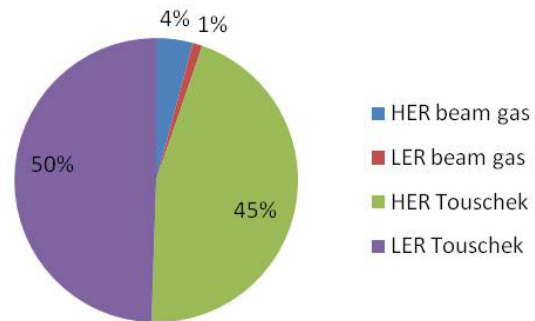


Figure 2.15: The fraction of background source(SVD at SuperKEKB).

detector layout of the SVD and the PXD. Inner two layers are replaced by PXDs and outer 4 layers are the same silicon strip detectors as the Belle SVD. The readout electronics of the Belle II SVD is based on the APV25 chip that has 50 ns of shaping time. This is much shorter than that of the Belle SVD readout based on the VA1TA chips, 800 ns. Detector configuration is shown in Table 2.6 and there are 6144 read out strips in the 1st layer.

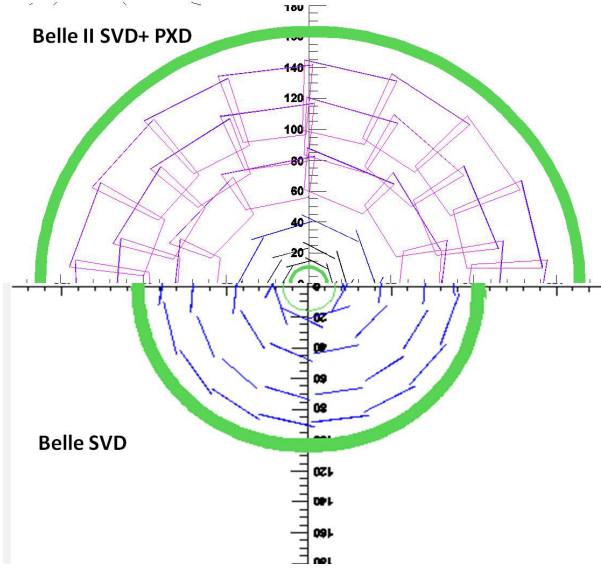


Figure 2.16: The layout of the SVD of Belle (bottom) and SVD/PXD of Belle II (top). Innermost layer of Belle II is replaced by PXD and located smaller radius than Belle.

Layer	Radius (mm)	strip number p-side	strip number n-side
3	38	12288	12288
4	80	23040	15360
5	115	43008	28672
6	140	65280	43520

Table 2.6: Detector configuration of the Belle II SVD, the radius of the straight part (not slanted), and strip number of the p-side (parallel to the z axis), and n-side (perpendicular to the beam axis).

SVD occupancy is calculated with these parameters by

$$\text{Occupancy} = (\text{Hit}/\text{trigger}) \times \frac{(\text{shaping time})_{\text{Belle-II}}}{(\text{shaping time})_{\text{Belle}}} \frac{1}{\#\text{Strips}}, \quad (2.7)$$

and the occupancy of 1st layer of the Belle II SVD is estimated to be $6.6 \pm 0.6\%$. From the Belle experience, the requirement for the Belle II SVD is that the occupancy should be less than 10%. The estimated background level at SuperKEKB satisfies this requirement.

The beam background on the PXD is also estimated from the estimated SVD hit per trigger. The PXD has 3.2M pixels in the first layer and total readout time is $20 \mu\text{s}$. The read out time of SVD is $\sim 2 \mu\text{s}$. Assuming the same particle hits on the PXD, the occupancy of the PXD is estimated to be $2.0 \pm 0.2\%$. In this estimation, low momentum particles and low energy gamma from synchrotron radiation or bremsstrahlung are not considered. The PXD is also sensitive to these low energy particles because the PXD is located closer to the IP than innermost layer of the Belle SVD therefore we can't state if the PXD is tolerable or not to total beam background.

We also estimate the occupancy in the case if we set a threshold to exclude low energy hits. The $k_{\text{beam-gas}}$, k_{Touschek} and estimated background at SuperKEKB if we use the Belle SVD at the same place under the SuperKEKB conditions are shown in Table 2.7. The expected occupancy at the 1st layer of the Belle II SVD and 1st layer of the PXD are estimated to be $1.2 \pm 0.2\%$ and $0.38 \pm 0.06\%$ respectively. This occupancy without low energy hits is used for checking the simulation of KEKB (chapter C).

	$k_{\text{beam-gas}}$ (hits·min/mA)	k_{Touschek} (hits·min/mA)	hits at SVD 1st layer (hits/trigger)
HER	120 ± 120	0.52 ± 0.08	230 ± 130
LER	6.6 ± 2.7	2.6 ± 0.4	970 ± 140
total	-	-	1200 ± 200

Table 2.7: $k_{\text{beam-gas}}$ and k_{Touschek} for SVD hit(> 3000 electron-hole) and expected SVD hit if we put the same SVD at the same place as Belle under the conditions of SuperKEKB(> 3000 electron-hole).

2.5.5 TOF/TOP

Total TOF/TSC trigger single rate, coincidence of TOF counter hit and TSC scintillation counters hit, is used for the estimation of the TOP background. The TOF design is shown in Figure 2.17. The TOF system consists of 64 TOF/TSC modules. Each module contains 1 TSC and 2 TOF counters. The trigger is created by taking coincidence of each TSC hit with any of the four PMTs of TOF counters. If there are more than two hits at different counters at the same

time, only one trigger is created. Thus the trigger rate is smaller than real hit rate. The hit rate with multiplicity > 2 is less than 3% of the hit rate with multiplicity = 1.

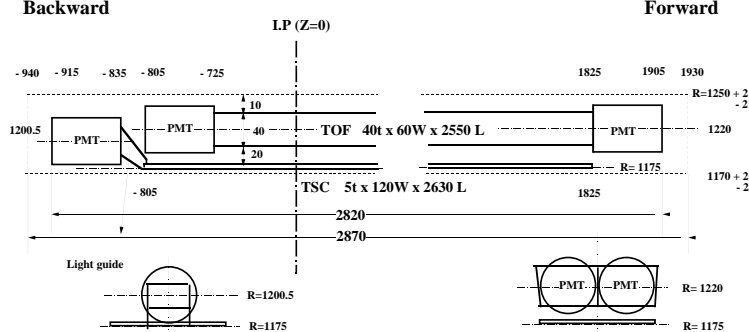


Figure 2.17: Design of the TOF/TSC module.

The relation between TOF/TSC trigger single rate scaled by beam current and the inverse life time is shown in Figure 2.18. The $k_{\text{beam-gas}}$ and k_{Touschek} are obtained based on this information. Each parameter and calculated background at SuperKEKB are shown in Table 2.8. If we use the Belle TOF at the same place under the SuperKEKB condition the expected background is ~ 2.9 MHz. Figure 2.19 is the pie graph of estimated background fraction. The main background source is the Touschek effect, about 99%. Touschek background on TOF from the HER is larger than from the LER.

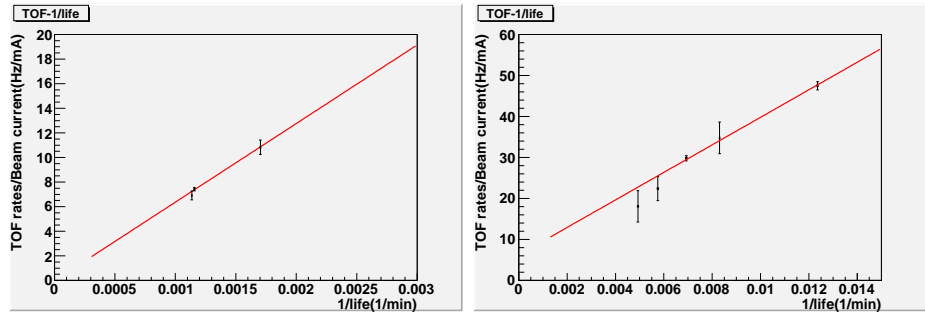


Figure 2.18: TOF hit rate scaled by beam current versus inverse beam life time for HER (left) and LER (right) during beam size scan. The mask setting is V-close.

In the case of Belle II, the TOP counter is used for barrel PID instead of the TOF. The TOP counter is designed to work under 20 times higher background level than that of Belle. Here, "background level of Belle" is estimated by simulation [12]. From the simulation, 1-4 coincidence trigger rate, hit both TSC

	$k_{\text{beam-gas}}$ (Hz·min/mA)	k_{Touschek} (Hz·min/mA)	TOF hit rate (MHz)
HER	6300 ± 4600	6400 ± 1100	1.7 ± 0.3
LER	8400 ± 1700	3400 ± 200	1.2 ± 0.1
total	-	-	2.9 ± 0.3

Table 2.8: $k_{\text{beam-gas}}$ and k_{Touschek} for TOF hit rate and expected TOF hit rate if we put the TOF at the same place as Belle under the conditions of SuperKEKB.

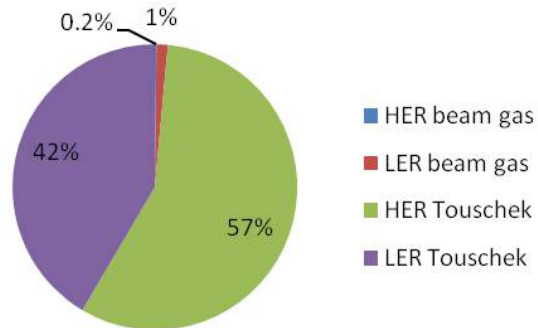


Figure 2.19: The fraction of background source(TOP at SuperKEKB).

and 4 of one TOF, by spent electron(including bremsstrahlung and Coulomb scattering) is estimated for several threshold levels. Hence we have to know the threshold level of TOF.

The threshold value of the TOF of Belle was set at 0.1 MIPs (the unit of energy deposit by a minimum ionization particle) at early period of the experiment. Deterioration of the scintillator causes attenuation of ADC values of MIP energy in the forward and backward region. This effect is checked in Exp.73 runs 792-914 [13]. If there is no attenuation, in the case a light source is just in front of the PMT, the ADC values for a MIP particle would be around 350 and the threshold is at 50, corresponding to $50/350 = 0.14$ MIPs. On the other hand, the attenuation factor is $\sim 0.4(0.7)$ for a forward(backward) PMT. If the light source is in a middle of the counter, ADC value corresponds to 0.2 - 0.35 MIPs. In our study, we assume the threshold value to be around 0.3 MIPs because the trigger requires two end PMTs signals and most of light source is in the middle of a counter. The TOF hit rate is estimated to be ~ 150 kHz if the threshold level is 30% of the energy deposit of MIP. Therefore, the tolerable background level of the TOP corresponds to the TOF trigger rate of ~ 3 MHz (0.3 MIPs threshold). The estimated background level of 2.9 MHz (0.3 MIPs threshold) is almost the same level of 3.0 MHz. If we assume all background particles are from spent electrons, the expected background can be critical for the TOP counter. The TOP counter should have safety factor to tolerate this estimated background.

From the TOF simulation, although the main spent electron background incident on the TOF surface is gamma ($\sim 90\%$), the main source creating hits at the TOP is e^- . To have a better estimation, we have to understand the momentum distribution and kind of incident particle(gamma or e^{+-}) of beam background. We also have to know other charged particle background levels.

2.5.6 ECL

The total energy deposit of particle hits above 1 MeV at the ECL is used for the estimation of the ECL background. Random trigger data during the Touschek study is used for this analysis. Not only the total background but also the background of forward, backward endcap and barrel part is estimated.

The relation between ECL energy deposit scaled by beam current and the inverse life time for each region are shown in Figure 2.20 (HER) and Figure 2.21 (LER). The $k_{\text{beam-gas}}$ and k_{Touschek} of each region are obtained based on the information. The evaluated parameters and estimated background if we put the same ECL at the same place under the SuperKEKB condition are shown in Table 2.9 and 2.10. Figure 2.22 is the pie graph of estimated background fraction at whole ECL. The main background source is the Touschek effect, about 98%.

We consider the effect of this expected background on the Belle II ECL. The crystal of the ECL is assumed to be the same CsI(Tl) as the Belle ECL. The ECL makes clusters with 25 cells if the energy deposit at a center cell is > 10 MeV. If total energy of a cluster is over 20 MeV, the cluster is defined

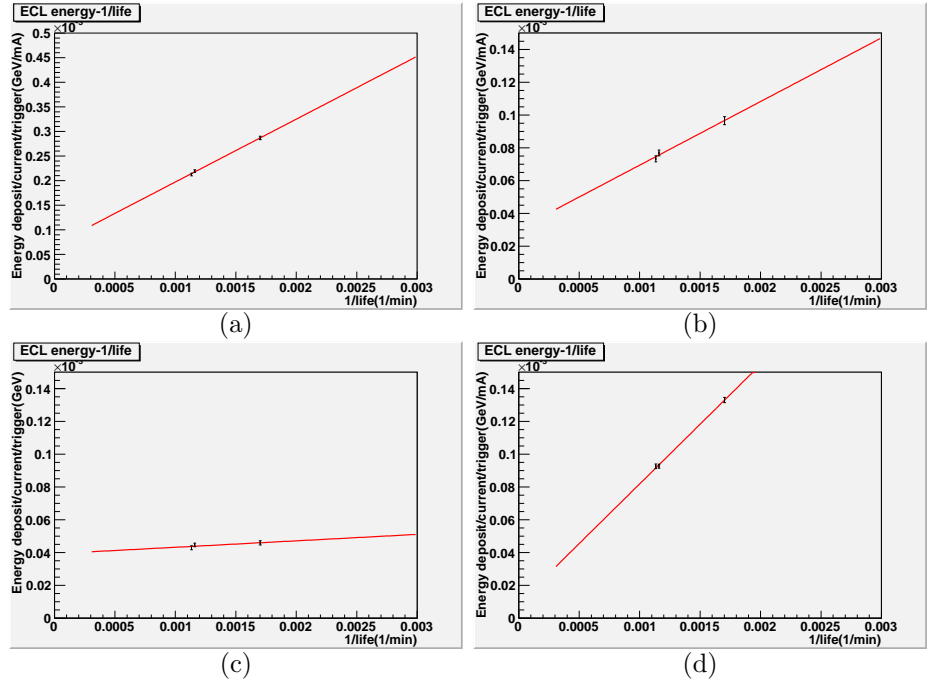


Figure 2.20: ECL energy deposit scaled by beam current versus inverse beam life time for the HER during beam size scan. (a) Whole ECL. (b) Forward region. (c) Backward region. (d) Barrel region.

The mask setting is V-close.

HER	$k_{\text{beam-gas}}$ (GeV·min/mA)	k_{Touschek} (GeV·min/mA)	ECL(Belle) energy deposit (GeV/trigger)	ECL(Belle II) energy deposit (MeV/trigger/crystal)
Forward	0.15 ± 0.1	0.039 ± 0.005	10 ± 1	0.9
Backward	0.14 ± 0.14	0.004 ± 0.003	1.0 ± 0.9	0.1
Barrel	0.10 ± 0.04	0.073 ± 0.003	19 ± 1	0.4
Total	0.36 ± 0.25	0.128 ± 0.007	34 ± 2	0.6

Table 2.9: $k_{\text{beam-gas}}$ (column 1) and k_{Touschek} (column 2) for ECL energy deposit (HER). Expected ECL energy deposit from HER when we put the same ECL at the same place as Belle under the conditions of SuperKEKB (column 3). Expected energy deposit at each crystal of the Belle II ECL with wave form fitting and shorter shaping time at each region assuming uniform energy deposit to all crystals (column 4).

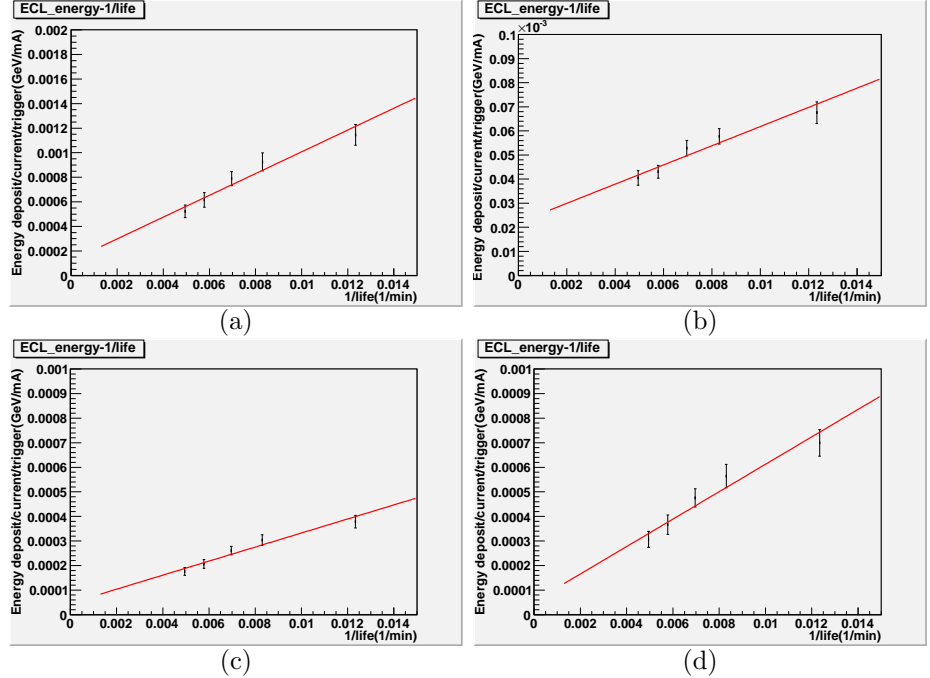


Figure 2.21: ECL energy deposit scaled by beam current versus inverse beam life time for the LER during beam size scan. (a) Whole ECL. (b) Forward region. (c) Backward region. (d) Barrel region.

The mask setting is V-close.

LER	$k_{\text{beam-gas}}$ (GeV·min/mA)	k_{Touschek} (GeV·min/mA)	ECL(Belle) energy deposit (GeV/trigger)	ECL(Belle II) energy deposit (MeV/trigger/crystal)
Forward	0.022 ± 0.005	0.004 ± 0.0007	1.5 ± 0.3	0.2
Backward	0.066 ± 0.007	0.029 ± 0.004	10 ± 1	1.5
Barrel	0.099 ± 0.048	0.056 ± 0.008	21 ± 3	0.5
Total	0.19 ± 0.08	0.089 ± 0.013	33 ± 2	0.5

Table 2.10: $k_{\text{beam-gas}}$ (column 1) and k_{Touschek} (column 2) for ECL energy deposit (LER). Expected ECL energy deposit from LER when we put the same ECL at the same place as Belle under the conditions of SuperKEKB (column 3). Expected energy deposit at each crystal of the Belle II ECL with wave form fitting and shorter shaping time at each region assuming uniform energy deposit to all crystals (column 4).

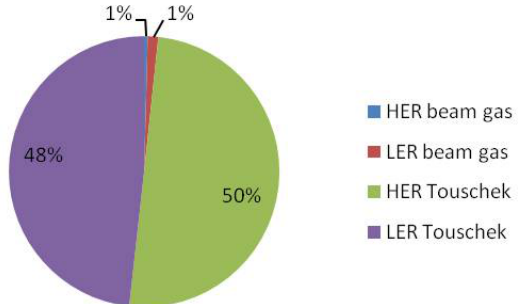


Figure 2.22: The fraction of background source (ECL at SuperKEKB).

as a hit. In the Belle II ECL, shaping time is changed from $1 \mu\text{s}$ to $0.5 \mu\text{s}$ and wave form fitting is used to reduce these backgrounds. The time between trigger time ($t_{trigger}$) and peak time (t_0) is measured by wave form fitting. The distribution of $t_0-t_{trigger}$ for signal and background have been simulated [14]. We can reduce background by setting a time window. For example, if we apply an energy-dependent timing cut of $|t_0-t_{trigger}| < 5000 \text{ ns}/(\text{E/MeV})$, the fake clusters are suppressed to $1/7$ by the shorter shaping time and the wave form fitting analysis. Here we assume that the beam background has a uniform time distribution because time interval between two bunches is of ns order while the time resolution of the ECL is of μs order. The timing cut is energy-dependent because the time resolution of the ECL depends on the particle energy [15]. The inefficiency due to time cut for different background level was also studied [14]. From this study, we can keep the efficiency of the cut for real photons at more than 90% for photon energies above 20 MeV for the same background of Belle. If the background level is larger than that of Belle, the efficiency will decrease. In this case, we need to increase the photon threshold, 30 MeV for the case of 20 times larger background, to keep the same efficiency level. Thus, a possible background level on the Belle II ECL is $\sim 9 \text{ GeV/trigger}$ after the timing cut with keeping real photon finding efficiency for above arbitrary photon threshold energy.

Assuming uniform energy deposit on each crystals, estimated energy deposit to one crystal is calculated by simply dividing by crystal number at each region, 1152 at forward end cap, 6624 at barrel and 960 at backward endcap region (column 4 of Table 2.9 and 2.10). We can see that HER (LER) mainly affects on the forward (backward) endcap. The energy deposit at one crystal is expected to be less than 1.5 MeV/trigger/crystal on average.

2.6 Conclusion

We performed a machine study to understand Touschek and beam-gas background and to estimate beam background at Belle II. We found that the background is linearly dependent on the vertical beam size as is expected. Touschek background which is expected to be main background source and beam-gas background at Belle II are estimated for each of the sub-detectors, PXD, SVD, CDC, TOP, and ECL (Table 2.11). In this study, the effect of other backgrounds are not taken into account. The main background source comes from Touschek scattering from the LER for inner tracker. Touschek scattering from the HER also has a great effect on the Belle II detector, especially in the TOP and the ECL. All detectors except the PXD and TOP are confirmed to work under the estimated beam background level. We have to take into account low energy particles and gamma for the PXD background. The estimated TOP background is almost matches the tolerable limit. TOP should be designed to work under worse background levels.

	Belle nominal (Exp.61)	Belle detector under SuperKEKB condition
SVD/PXD hit(hits/trigger,E>10keV)	150	6500
CDC current(μ A)	13	440
Total ECL energy deposit(GeV/trigger)	7.1	66
TOP(TOF trigger rate)(kHz)	90	2900

Table 2.11: Background of each sub-detector in Exp.61 and expected background at SuperKEKB using the current Belle detector under the conditions of SuperKEKB.

Chapter 3

Cooling test of the beam pipe

In this chapter, we present the cooling system for the straight part of the beam pipe. The paraffin cooling system has been successfully working for Belle. In Belle II, there is less space in the forward region because the crossing angle is larger and final focusing magnets are closer to the IP than Belle. The manifold for the cooling system in the forward region can conflict with the PXD readout electronics, cables for readout and the cooling system. Moreover, increase of the image current on the beam pipe is expected because of higher beam current and smaller beam pipe radius.

We pursue possibility of a return cooling system which doesn't have a manifold in the forward region. We are now thinking about a one-way cooling system. We also discuss its cooling capability.

3.1 The beam pipe design

The beam pipe of the IR will be composed of Beryllium at the straight part and Tantalum at the crotch part. This is because we have to use less material within the detector acceptance and more material outside of the acceptance to stop background particles. These two regions are connected by brazing with stainless steel. The straight part is a double pipe of Beryllium and coolant flows through the gap between two beam pipe walls. The physics properties of beam pipe materials are listed in Table 3.1.

There are two possible designs for the cooling system, return cooling and one-way cooling system (Figure 3.1). In the return cooling system, similar to that used in Babar at SLAC, coolant enters from the backward end, returns at the forward end, and exits from the backward end again. The merit of this design is that forward manifold is not needed and more space for the PXD and cables for readout and cooling system is available. The disadvantage is that cooling capability at the return end can be worse than other region. Moreover,

	Be	SUS304	Ta	Al
density (g/cm^3)	1.84	7.93	16.7	2.70
specific heat ($\text{J}/\text{kg}/{}^\circ\text{C}$)	1778	590	142	900
linear expansivity ($10^{-6}/{}^\circ\text{C}$)	11.6	17.3	6.3	23
radiation length (cm)	35.28	1.72	0.4094	8.897
Thermal conductivity ($\text{W}/\text{m}/\text{K}$)	200	16.7	57.5	237

Table 3.1: Physics properties of beam pipe material. Aluminum is used for the beam pipe mockup.

the return cooling system needs twice the coolant gap than a simple one-way cooling system with the same flow rate. Degradation of the impact parameter resolution due to thicker paraffin gap is discussed in section 4.2.6. The cooling capability is tested by a mockup test in section 3.7.

In the one-way cooling system, similar to that used at Belle, coolant enters from the backward end, and exits from the forward end. This design is simple and cooling capability at the backward end is expected to be better than the return cooling system. We can lessen the coolant gap if we operate the system with the same flow rate as the return cooling system. Its disadvantage is manifold space in forward region.

We are now considering applying the one-way cooling system, and preparing a new beam pipe mockup. We discuss the cooling capability of the one-way cooling system in section 3.8.

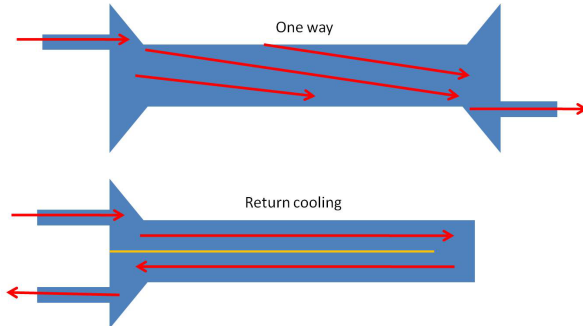


Figure 3.1: Two possible cooling schemes: one-way (top) and return (bottom).

3.2 Heat sources and requirement for cooling capability

There are three types of heat source at the IP chamber: Higher Order Mode(HOM), wall current, and synchrotron radiation hits.

- HOM

When beam bunches run through a component with a sudden variation of diameter, bellows or mask etc., electromagnetic field attached to the beam bunch is scattered or trapped. The scattered component will move away from the region and don't contribute to heating of the IR. On the other hand, trapped components stay in the region and can be heat source.

Beam loss energy by HOM is calculated by

$$P = \frac{W}{T} = \frac{kq^2}{T} = I_0^2 k T, \quad (3.1)$$

where W is energy deposit per 1 pass at the component, T is the bunch interval = 4 ns, q is the charge of bunch, I_0 is the beam current = 3.6 A / 2.6 A (LER/HER), and loss factor k is defined as W/q^2 . The loss factor for current IP chamber design is calculated by K. Shibata to be $\sim 3 \times 10^{-3}$ V/pC. Thus the beam energy loss is 160 W / 80 W (LER/HER). The attenuation length of a micro wave through a Cu wave guide is ~ 200 -400 m [16]. Wave length of HOM can be considered as order of bunch length ~ 5 mm and this is micro wave region. HOM energy deposit at 0.2 m of the IP chamber is less than ~ 1 W.

- Image current

Charged particles through the beam pipe drag charge on the surface of the beam pipe and image current is induced. Energy loss by image current can be calculated by [17]

$$\frac{W_L}{L} = \frac{\Gamma(3/4)}{4\sqrt{2}\pi^2} \frac{q_B}{\epsilon_0 a} I \sqrt{\frac{\rho_R}{Z_0 \sigma_z}} \frac{1}{\sigma_z} [W/m], \quad (3.2)$$

where Z_0 is the characteristic impedance of vacuum = 377 Ω , a is the duct radius = 1×10^{-2} m, ρ_R is the resistivity = 2.26×10^{-8} $\Omega \cdot \text{m}$ for Au, I is the beam current, q_B is the charge of the bunch = $1.45 / 1.05 \times 10^{-8}$ C (LER/HER), and σ_z is the bunch length. Thus energy loss by image current is W_L/L is $2.17 / 1.49 \times 10^2$ W/m (LER/HER) and expected heat at the straight part of the IP chamber (20 cm) is ~ 73 W.

- Synchrotron radiation hit

To avoid direct synchrotron radiation hit, the beam pipe has a taper design with saw tooth in crotch part. A simulation study to evaluate the energy deposit of synchrotron radiation at the IR was performed and the expected hits at the straight part was ~ 4 W.

From these expectations, the calculated heat of the straight part of the IP chamber is ~ 80 W.

3.3 Coolant selection

The requirement for the IP chamber coolant is as follows.

- Long radiation length
- Small viscosity (to achieve enough flow rate)
- High heat capacity
- No corrosive effect on Beryllium

At the first operation of Belle, Helium was used for the IP chamber cooling system. We have to carefully control humidity if we use a gas coolant. In fact, the first Belle beam pipe was broken because of high humidity. Moreover gas coolant needs more space for channel than liquid coolant.

Water seems to be good coolant because of its good cooling ability, high heat conductivity, heat capacity, and low viscosity. It was used in the cooling system of the CLEO 2.5 beam pipe and the Babar beam pipe. The disadvantage of water is the possibility of it corroding the Beryllium. Beryllium can be corroded when the cooling system is contaminated by chlorides or sulfides. If we use water for coolant, the Beryllium beam pipe will be guarded by a single-component epoxy, such as BR127, as done in Babar [18].

Paraffin is a kerosene like fluid, a mixture of straight alkane, used for the Belle SVD and the CLEO cooling system. Mixing of N=10 and 15 straight alkane is used for the Belle system and PF200 is used for the CLEO system [19]. These two types of paraffin have similar physics properties. PF200 and paraffin used for the Belle system are discontinued now. We can purchase paraffin which contains mainly N=10 linear alkane, decane, instead (N=10 : 98%, N=11, 9 < 2%). The merit of this "new" paraffin is smaller viscosity. Its disadvantage is lower flash point. We are currently considering this paraffin. The basic physics properties of these coolants are shown in Table 3.2.

	Paraffin(decane)	H ₂ O	PF200[19]	He
Density at 15 °(g/cm ³)C	0.734	1.00	0.78	1.78×10^{-3}
Specific heat (J/g K)	2.21	4.19	2.46	5.23
Kinematic viscosity at 30 °C (cSt)	1.1[20]	0.8	2.41	109
Radiation length (cm)		36.1	52	5.67×10^5
Flash point (°C)	51	-	93	-

Table 3.2: Physics properties of various coolants.

3.4 Requirement for cooling system

In this section, we discuss the requirement for the flow rate due to pressure drop and cooling capability. We perform a mockup test to check that our system satisfies these requirements in section 3.7.

3.4.1 Pressure drop

If the Reynolds number (Re) is less than 2000-3000, the flow is expected to be laminar otherwise flow is turbulent. The Reynolds number is defined by

$$Re = \frac{vD}{\nu}, \quad (3.3)$$

where v is the kinematic velocity, D is the effective diameter and ν is the kinematic viscosity. Effective diameter is defined as

$$D = 4 \frac{\text{cross sectional area}}{\text{perimeter length}}. \quad (3.4)$$

Pressure drop for a laminar flow between two plates is calculated by [21]

$$\Delta P = 12 \frac{\nu u L}{b^2}, \quad (3.5)$$

where b is the gap size between two plates. Pressure drop for laminar flow in a straight tube can be calculated by Fanning's equation,

$$\Delta P = 2 f \rho u^2 \frac{L}{D}, \quad (3.6)$$

where u is the average velocity, L is the length of flow, and f is the friction factor.

When laminar flow condition, f is given by Poiseuille equation

$$f = 16/Re. \quad (3.7)$$

When turbulent flow condition, f is given by Carman's equation or approximation form Swamee-Jain equation,

$$f = 0.0626 * \left[\log_{10} \left(\frac{e}{3.7D} + \frac{5.74}{Re^{0.9}} \right) \right]^{-2}, \quad (3.8)$$

where e is the roughness of surface. Application range of Swamee-Jain equation is $3 \times 10^3 < Re < 3 \times 10^6$. The pressure drop is not continuous between laminar and turbulent condition. When the flow is in this transition region ($Re = 2000-3000$), the condition can be oscillate between laminar and turbulent. This oscillation stresses the IP chamber. Thus the operation in the transition region has to be avoided.

Belle II IP chamber is designed to withstand pressure drop up to 0.1 MPa. The effective diameter of the straight part of the return cooling system with

0.5 mm paraffin gap is 1 mm. Expected pressure drop by paraffin flow is analytically calculated from Eq.(3.5) (Figure 3.2). We assume the viscosity of decane at $T = 20^\circ\text{C}$, 1.26 cSt. The Reynolds number is less than 2000 and flow condition is laminar. It seems that expected pressure drop is less than 0.1 MPa and it satisfies the requirement even if flow rate is ~ 2 l/min. In this calculation, however, pressure drop of manifold and effect of the return end are not taken into account. Sudden variation of diameter or direction of flow path causes much pressure drop. We have to check pressure drop with a realistic mockup.

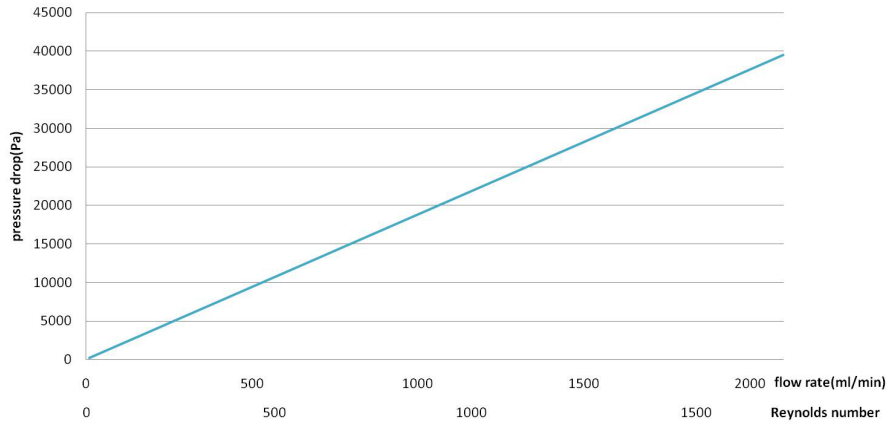


Figure 3.2: Pressure drop of paraffin flow through the return cooling beam pipe mockup calculated by Eq.(3.5) as a function of flow rate and Reynolds number. Total flow length is 40 cm. $T = 20^\circ\text{C}$.

3.4.2 Cooling capability

If heat conduction between coolant and the beam pipe is large enough, heat removed by coolant is calculated as

$$W = \Delta T \times r \times F[W], \quad (3.9)$$

where ΔT is the difference in temperature between entrance and exit of the cooling section, r is the specific heat, and F is the flow rate. This equation means that cooling capability depends only on the flow rate of the coolant. The heat conduction between coolant and the beam pipe has not been simulated but we assume that the heat conduction is large enough. If we allow $\Delta T = 5^\circ\text{C}$, 0.6 l/min is needed to remove 80 W heat. Thus flow rate of > 0.6 l/min is required and 1 l/min seems to be sufficient for our system.

3.5 Setting for Cooling test

We make an aluminum mockup of the IP chamber for the return cooling system. The mockup is composed of the manifold part and the straight part which will consist of Beryllium for the real IP chamber. The straight part is 20 cm length and 10 mm inner radius with 0.5 mm gap for paraffin channel. The manifold part is larger than the realistic design. The paraffin gap is smaller than the realistic design of 1 mm gap. We check its cooling capability (section 3.7). The mockup is connected to a pump, flow monitors, temperature monitors, pressure monitors, and a chiller system by plastic tube with inner diameter of 4 mm, as Figure 3.3 shows. The temperature of coolant is controlled by the chiller system. The flow rate is controlled by the bypass valve. Here, used components are listed.

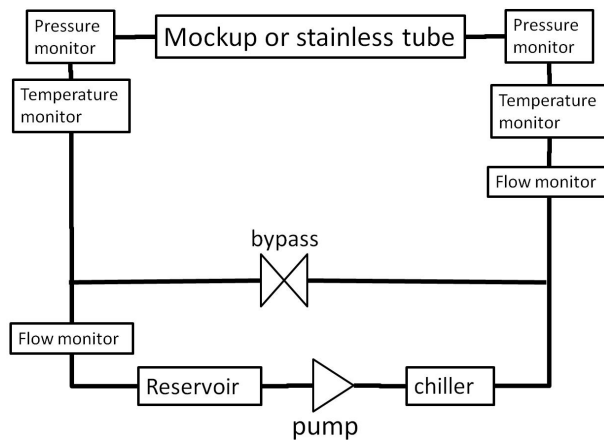


Figure 3.3: Schematic drawing of the cooling test setup.

- Pump

We use a magnet gear pump produced by Nikkiso(MG213). Magnet pump is seal-less at shaft so that risk of leaking is very small.

- Flow meter

We use impeller flow meters, ND05-N ATAAC produced by Aichi tokei denki. The sensor measures rotation frequency of impeller which set at the flow path. The detection principle is simply mechanical so that sensor can be used for many kinds of fluid. The range is from 0.3 to 3.0 l/min. We check the accuracy of the flow meter by measuring the time to fill up the 2 l reservoir. We find that the flow meter has accuracy of $\sim 10\%$.

- Pressure monitor

Diaphragm pressure monitors, AP-V80 produced by KEYENCE, are used.

The range of the sensor is from 0 to 1 MPa and analogue output range is 4 to 20 mA We used 200 ohm resistance for analogue output.

- Temperature monitor

Cu sheathed thermocouples are inserted in a plastic tube to measure the temperature of the flow directly. PT100 resistance temperature detectors are used to measure surface temperature of the mockup.

3.6 Viscosity of paraffin

The viscosity of paraffin is larger at lower temperature. The larger the viscosity of paraffin, the larger pressure drop in the IP chamber is. Mechanical strength of the beam pipe can bear less than 0.1 MPa of pressure drop. We have to confirm that the viscosity of paraffin is small enough to circulate paraffin at sufficient flow rate of ~ 2 l/min.

To measure the viscosity of paraffin we measure the pressure drop in a stainless steel straight tube. The setup is the same as shown in section 3.5 except that a 2 m stainless steel tube with inner diameter of 4 mm is connected instead of the mockup. If the fluid is in turbulent condition, pressure drop depends on the roughness of surface which is an unknown parameter. Thus we have to operate in laminar condition.

As for the condition of the study, the flow rate is set to 0.3 l/min and 0.45 l/min and the coolant temperature is set to possible temperature of 10 °C and 15 °C respectively. The flow rate is selected so that the paraffin flow is in laminar condition. The Reynolds number is calculated to be less than 2000, laminar flow, from the viscosity of literature value [20]

The results are shown in Table 3.3. Viscosity is calculated from Eq.(3.6). The Reynolds number calculated from the measured viscosity is also less than 2000 and the flow condition is laminar. The measured viscosity is plotted in Figure 3.4 together with the literature value of the viscosity of Decane. We found larger viscosity in lower temperature which agrees with the expectation.

The measured viscosity at 0.3 l/min seems to be larger than at 0.45 l/min. We should note that the flow rate of 0.3 l/min is almost less than the detection limit of the flow meter and measured flow rate at 0.3 l/min is not accurate.

The measured viscosity at 0.45 l/min is still larger than viscosity of Decane. This might be because that the paraffin that we used is a mixture of Decane and other straight alkane ($N = 11, 9$) which have different viscosity. The viscosity of straight alkane at 15 °C is 0.0013 Pa*s [22] and 0.00075 Pa*s [22] for $N = 11$ and $N = 9$ respectively. If content rate of $N = 11$ alkane is large, the viscosity of the paraffin is larger than that of Decane.

The pressure drop becomes higher for the higher viscosity coolant flow. This means that pressure drop of paraffin flow is expected to be higher than that of Decane flow. Expected pressure drop of paraffin flow through the return cooling beam pipe mockup is calculated for each flow rate assuming Decane viscosity(Figure 3.2). We again calculate the pressure drop assuming the worst

pressure drop condition in measured viscosity, $\nu = 0.002 \text{ Pa}^*\text{s}$ (Figure 3.5). In this condition, the Reynolds number is less than 2000 and the flow condition is laminar. Even if the viscosity is the highest value in the measurement value, pressure drop is less than 0.1 MPa at the flow rate of 2 l/min. It is confirmed that we can achieve paraffin cooling system with the flow rate of 2 l/min at $>0.1 \text{ MPa}$ of pressure drop.

Temperature (°C)	Flow rate (l/min)	ΔP (kPa)	ν (Pa*s)	Re
10.1	0.29 ± 0.03	3.1 ± 0.1	0.0020 ± 0.0002	580
9.9	0.45 ± 0.05	3.9 ± 0.3	0.0016 ± 0.0002	1080
13.9	0.28 ± 0.03	2.8 ± 0.3	0.0019 ± 0.0003	570
15	0.46 ± 0.05	3.4 ± 0.3	0.0014 ± 0.0002	1250

Table 3.3: Measurement of viscosity of paraffin. Measurement error is considered.

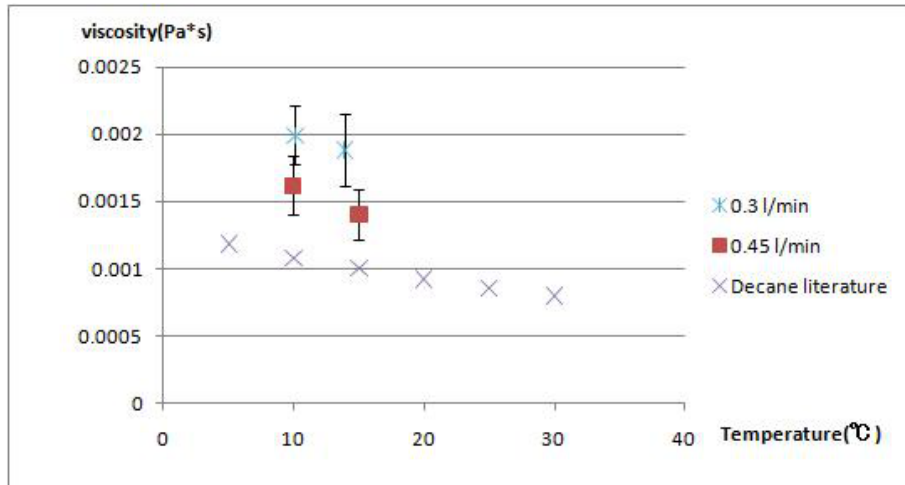


Figure 3.4: Measured viscosity and literature value of paraffin.

3.7 Test of return cooling system

We test cooling capability of return cooling system.

Figure 3.6 shows the schematic drawing of the mockup and temperature monitors. A heating wire generating 80 W heat is inserted in the mockup as a heat source. Five PT100 resistances are attached to the mockup surface (named

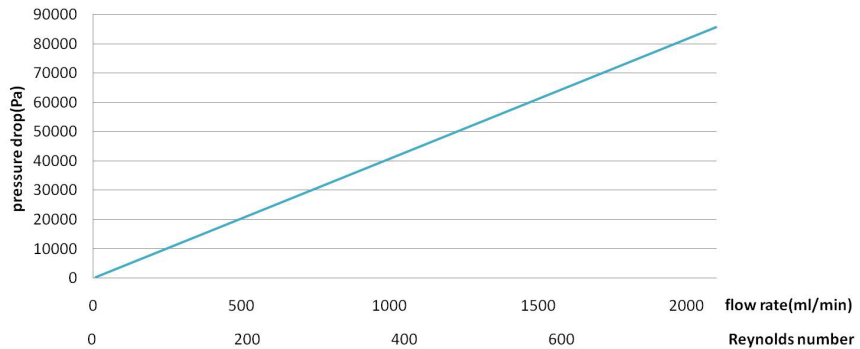


Figure 3.5: Pressure drop of paraffin flow through the return cooling beam pipe mockup as a function of flow rate or Reynolds number. Assumed viscosity is the worst pressure drop case, $\nu = 0.002 \text{ Pa}^*\text{s}$.

A, C-F) to measure the surface temperature. One resistance is located beside the heater in the beam pipe (named B). To insulate the mockup from circumstance heat, the mockup is placed inside a styrofoam box.

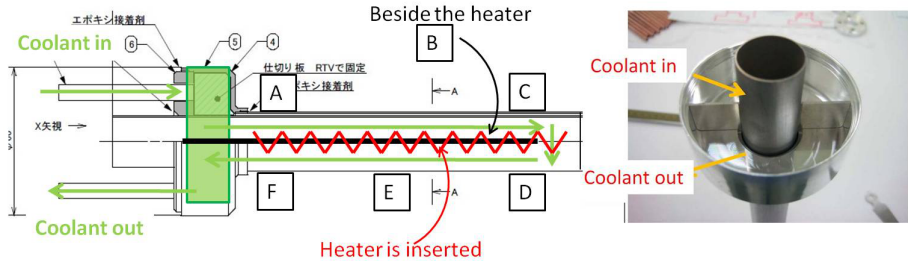


Figure 3.6: Schematic drawing of the IP chamber mockup. The symbols A-F describe the position of temperature monitors (PT100). The monitors A and C-F are attached to the mockup surface. The monitor B is inserted in the mockup.

The conditions of flow rate and temperature of the coolant are (a) 1 l/min and 20 °C, (b) 1.8 l/min and 20 °C, and (c) 1.8 l/min and 10 °C respectively. The expected Reynolds number of this system is less than 2000 (Figure 3.5) and the flow is laminar condition. Experimental procedure is as follows (Figure 3.7). The initial state is that heater is turned off and pump is turned on, then turn on the heater (1), turn off the pump (2), turn on the pump (3) and finally turn off the heater(4).

The surface temperature differences relative to the monitor A are shown

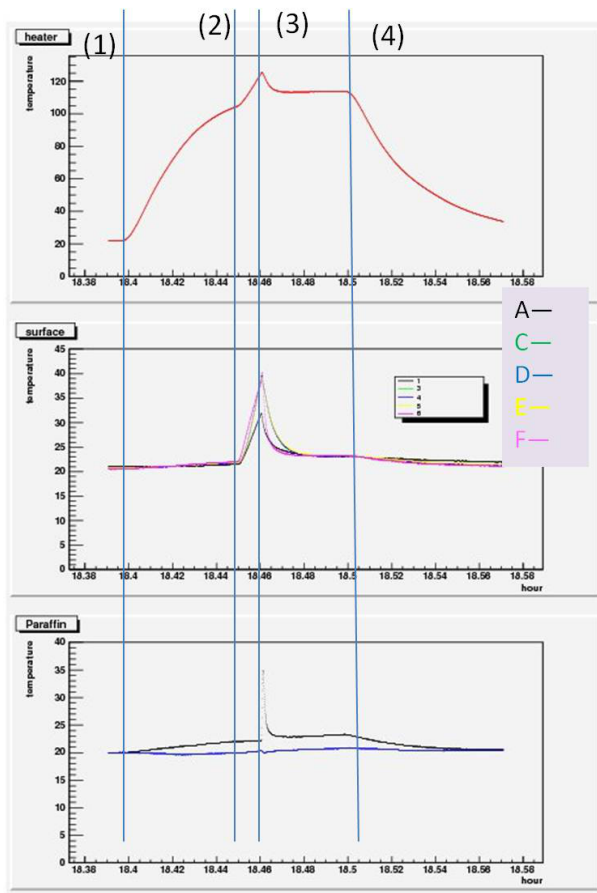


Figure 3.7: Flow rate is 1 l/min and paraffin temperature is 20 °C. Heater temperature (top), surface temperature (middle), and paraffin temperature (bottom, blue:enter, black:exit).

in Figure 3.8. To separate the heat of heater and others(environment etc.), temperature difference of initial state(before the point 1) relative to the monitor A is subtracted. We have worried that the return end couldn't be cooled enough, but such feature is not observed. The largest temperature difference is seen at the exit of the mockup. The temperature difference is less than $\sim 1^{\circ}\text{C}$. It is found that the mockup is cooled sufficiently.

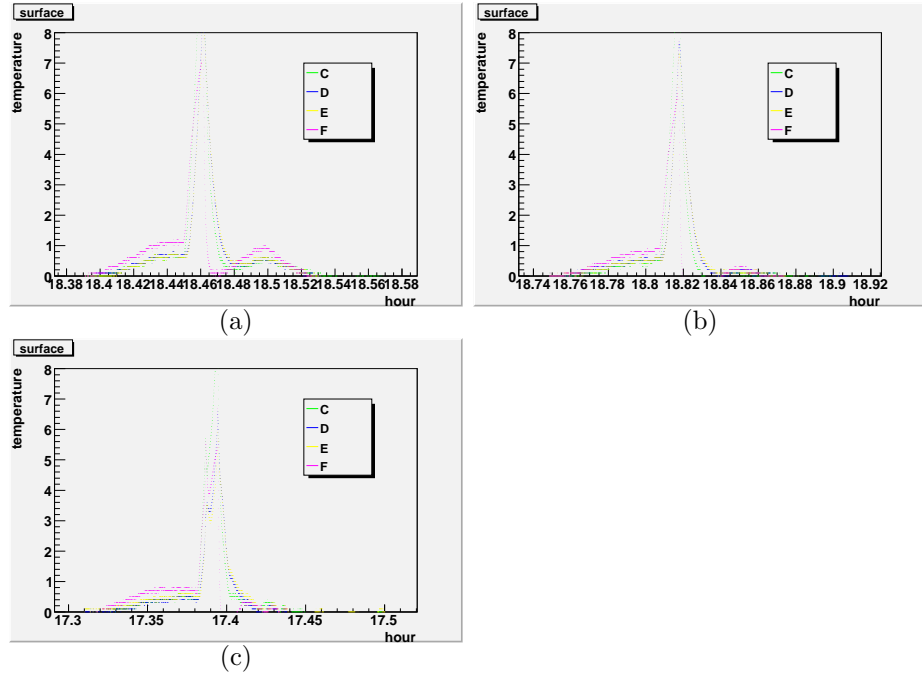


Figure 3.8: The surface temperature difference relative to the monitor A. (a) 1 l/min, 20°C (b) 1.8 l/min, 20°C (c) 1.8 l/min, 10°C.

The measured pressure drop and removed heat are listed in Table 3.4. The pressure drop is found to be less than 0.1 MPa and we can achieve up to 1.8 l/min for return cooling system with 0.5 mm gap. The expected pressure drop in section 3.6 is 40 kPa at 1 l/min and 75 kPa at 1.8 l/min. The difference between the expectation and measured value can be considered as the pressure drop at the manifold part. The pressure drop at the manifold is expected to be ~ 20 kPa at 1.8 l/min.

The heat removed by coolant is measured by temperature difference(ΔT) of paraffin between entrance and exit of the mockup. The plot between the point (3) and (4) in the bottom plot of Figure 3.7 is fitted by exponential function with offset (equilibrium temperature) to obtain equilibrium temperature. To

separate the heat of heater and others the temperature difference of initial state (before the point (1)) is subtracted from ΔT . Figure 3.9 shows the temperature difference by 80 W heat at each flow rate. The green line is the theoretical value calculated by Eq.(3.9) assuming 80 W heat. The measurement values are consistent with the theoretical value. It is confirmed that the heat conduction between aluminum and coolant is good enough. At SuperKEKB, the beam induced heat is expected to be ~ 80 W. We can remove 80 W heat with the temperature difference of $\sim 2.5^\circ\text{C}$ for 1 l/min or $\sim 1.5^\circ\text{C}$ for 1.8 l/min.

Flow rate (l/min)	Temperature ($^\circ\text{C}$)	ΔP (kPa)	ΔT ($^\circ\text{C}$)	Q (W)
1.0 ± 0.1	19.5 ± 0.1	39	2.5	69 ± 9
1.8 ± 0.2	9.4 ± 0.1	94	1.5	75 ± 7
1.8 ± 0.2	20.2 ± 0.1	87	1.6	80 ± 9

Table 3.4: The heat paraffin obtained through the mockup(Q) for each flow rate and temperature. The heat source is 80 W.

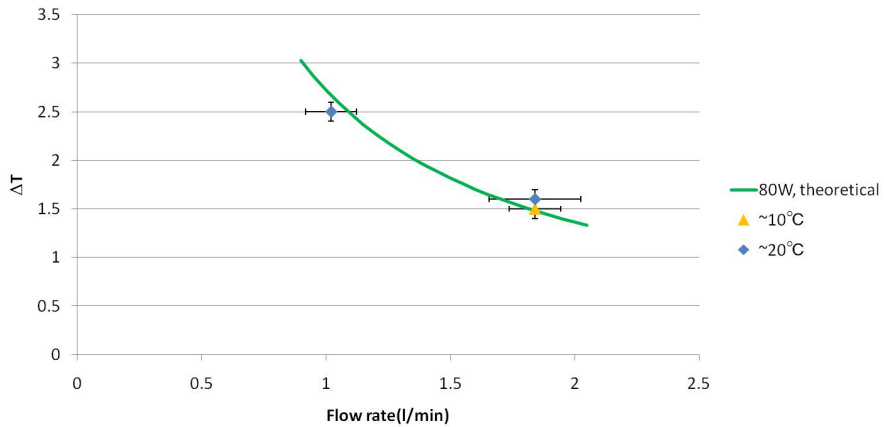


Figure 3.9: Temperature difference ΔT for each flow rate. Blue and orange points are measured ΔT for 80 W heat source. Green line is the theoretical value calculated by Eq.(3.9) assuming 80 W heat.

3.8 New beam pipe design

Current beam pipe design and the materials of the straight part are shown in Figure 3.10 and Table 3.5. The cooling scheme is one-way. paraffin gap is

1.0 mm at the SUS connection part and 0.8 mm at the Beryllium straight part, which is smaller than that of the return cooling system. The forward manifold is carefully designed not to conflict with the PXD.

To achieve the same cooling capability, we have to circulate the coolant at the same rate for both return and one-way cooling system if heat conduction between coolant and the beam pipe is large enough. Return cooling system therefore needs twice the paraffin gap than the one-way system because it has half the cross sectional area of the flow path than the one-way system with the same paraffin gap. We can decrease the paraffin gap with the one-way cooling system. The temperature difference between the entrance and exit of the cooling section is expected to be the same as the return cooling if the heat conduction is large enough. The expected temperature difference is ~ 2.5 °C to remove ~ 80 W heat if we circulate paraffin at 1 l/min.

If the flow rate is 1 l/min or 2 l/min and the viscosity is the worst case, 0.002 Pa*s (measured in section 3.6), the Reynolds number is 190 or 390 respectively. These flows are under the laminar condition. Expected total pressure drop is 1.4 or 2.7 kPa respectively. This rather small pressure drop is due to the larger paraffin gap than the mockup of the return cooling system and satisfies the requirement for the pressure drop. Although the manifold design is not fixed, the pressure drop at the manifold is considered as the same order as the return cooling system. It is expected that we can even flow 2 l/min.

We prepare a mockup of this straight part made of SUS (Figure 3.10). We will test the cooling capability with the mockup.

Material	Thickness
Au plating	10 μ m
Be inner wall	0.6 mm
gap for paraffin(return/one-way)	1.0/0.8 mm
Be outer wall	0.4 mm

Table 3.5: Material for the straight part of the beam pipe from innermost to outermost. Inner radius is 10 mm and total thickness is 2 mm. Paraffin gap of the one-way system is smaller than that of the return cooling system.

3.9 Conclusion

We measure the viscosity of the possible paraffin ($N=10$) coolant for the Belle II beam pipe cooling system. The measured viscosity of paraffin is small enough at 10 °C to circulate paraffin at 2.0 l/min. We test the cooling capability of the return cooling system with paraffin gap of 0.5 mm. The flow rate of 1.8 l/min is achieved at pressure drop of less than 0.1 MPa and 1 l/min flow rate is enough to remove 80 W heat with 2.5 °C temperature difference between incoming and outgoing paraffin.

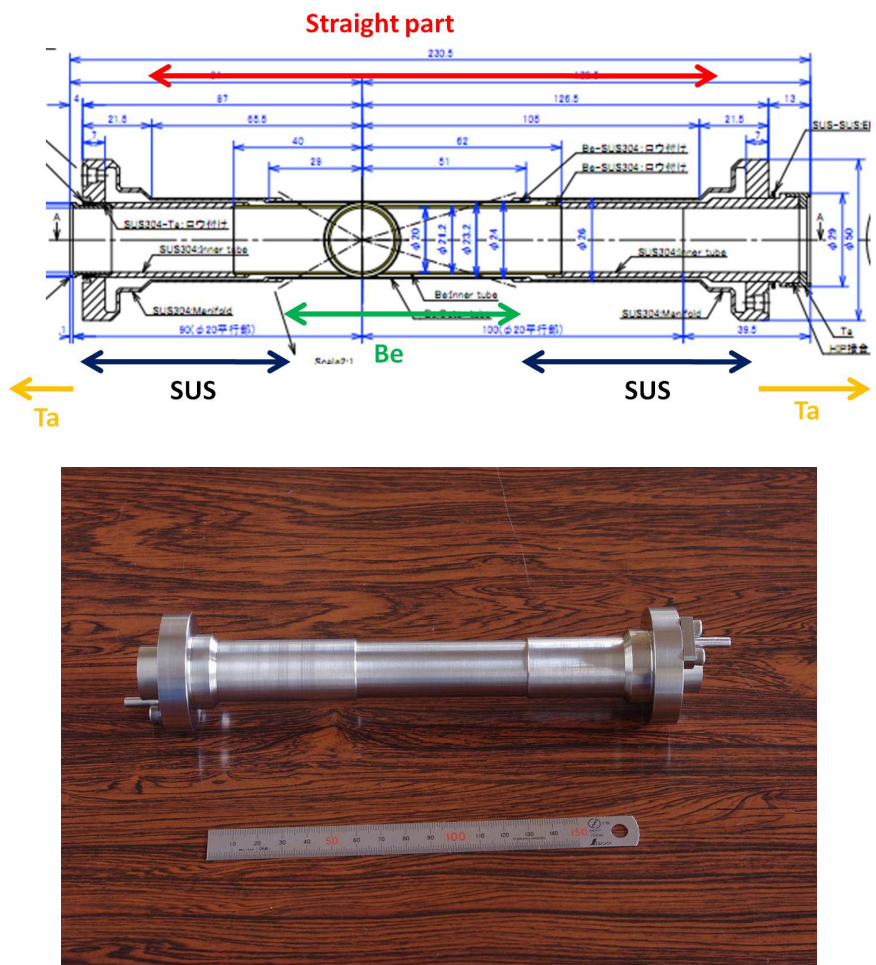


Figure 3.10: Current design of straight part of the beam pipe (top). The one-way cooling scheme is adopted. The mockup of the beam pipe with the one-way cooling system (bottom).

For the new beam pipe design, we are preparing the SUS mockup. The flow rate of 2 l/min is expected to be achieved with pressure drop of less than 0.1 MPa and cooling capability is also expected to be good. Expected cooling performance of both one-way and return cooling system is listed in Table 3.6.

	Return	One-way(expected)
ΔT at 1 l/min ($^{\circ}$ C)	2.5	2.5
Pressure drop at 1 l/min(kPa)	40	1.4
Flow condition	laminar	laminar
Paraffin thickness(mm)	1	0.8
Mockup test	done	not yet
Manifold	backward only	both forward and backward
Conflict with PXD	no	no (but still should pay attention)

Table 3.6: Expected performance of return and one-way cooling system.

Chapter 4

Tracking performance simulation study for SVD design

4.1 Slant and straight design

The SVD and PXD are detectors for measuring the interaction point accurately. In Belle II, there are two PXD layers at the innermost part and four SVD layers surround them. They cover 14 cm distance from the beam axis. To lay out 4 layers of the SVD, there are two possible designs: "slant" and "straight". Two designs are shown in Figure 4.1. The outer 3 layers of the slant design have cone type layers in the forward region (the polar angle $< 30^\circ$) and the shape of each ladder in this region is trapezoidal. On the other hand, the straight design covers the whole region with barrel type layers.

The merits and demerits of these two designs are listed below.

- The straight design has a simple layout and its alignment is easier than the slant design.
- In very forward region, the angle of incidence of a particle track is large and a particle needs to pass through more materials than the case of small angle of incidence. This causes more multiple scattering and degradation of position resolution. Low momentum particles are sensitive to this degradation. The material budget of these designs are studied by Z. Drasal (Figure 4.2[3]). It is clearly expected that slant design has less material in the forward region and therefore better resolution. No difference is seen in the azimuthal angle distribution of material between both designs. We assume uniform detectors in azimuthal angle and neglect the azimuthal angle difference.
- The space for readout cables and fixed-type masks that prevent a particle

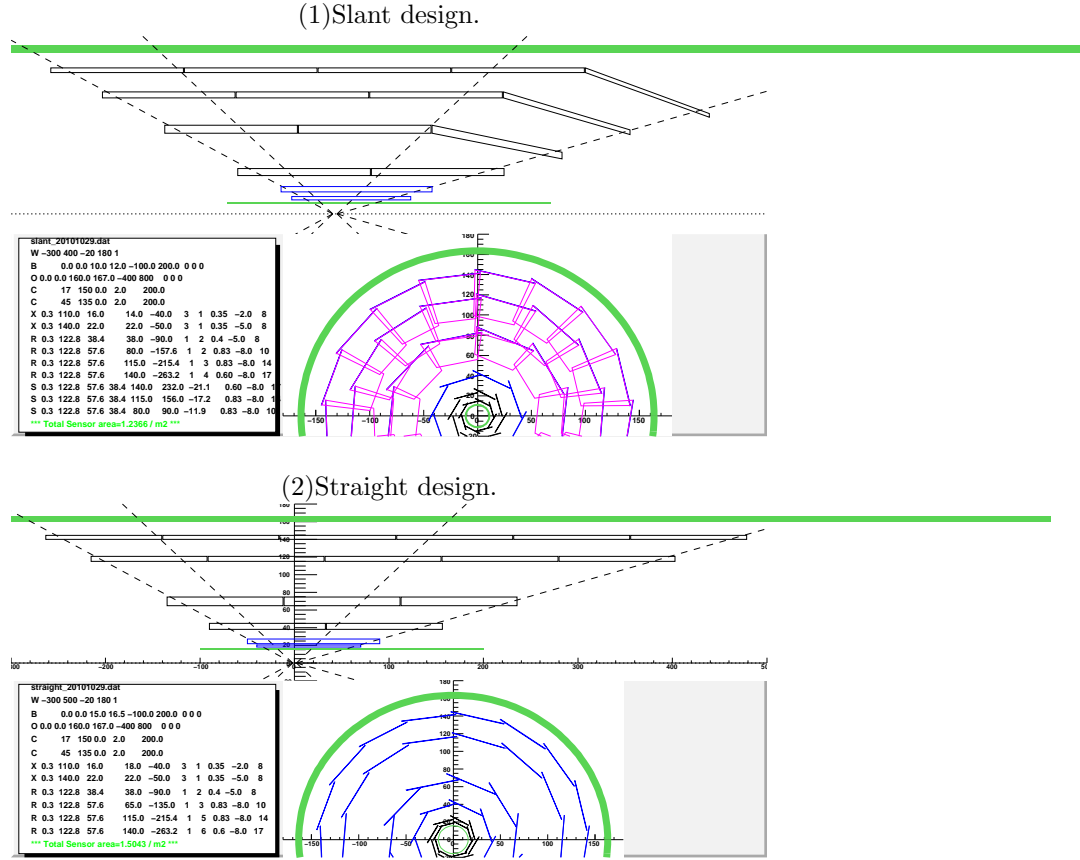


Figure 4.1: Two SVD designs.

background hitting at the detector is related to the SVD design. Detailed structure design of the slant design has been developed and so far we see no problem for the cabling space[23]. Based on the realistic design, the mask design should be optimized to shield beam background effectively, which is related to source position of incoming background particle which hit the Belle II detector and their amount. To understand the background environment and confirm the mask design simulation study is ongoing.

- The straight design is composed of 31 more ladders than the slant design. This means that additional cost is needed to construct the SVD of the straight design.

We have to take into account these merits and demerits for the choice of the design. To evaluate the second point (material effect in the forward region), we perform a simulation study and estimate the tracking parameter resolution.

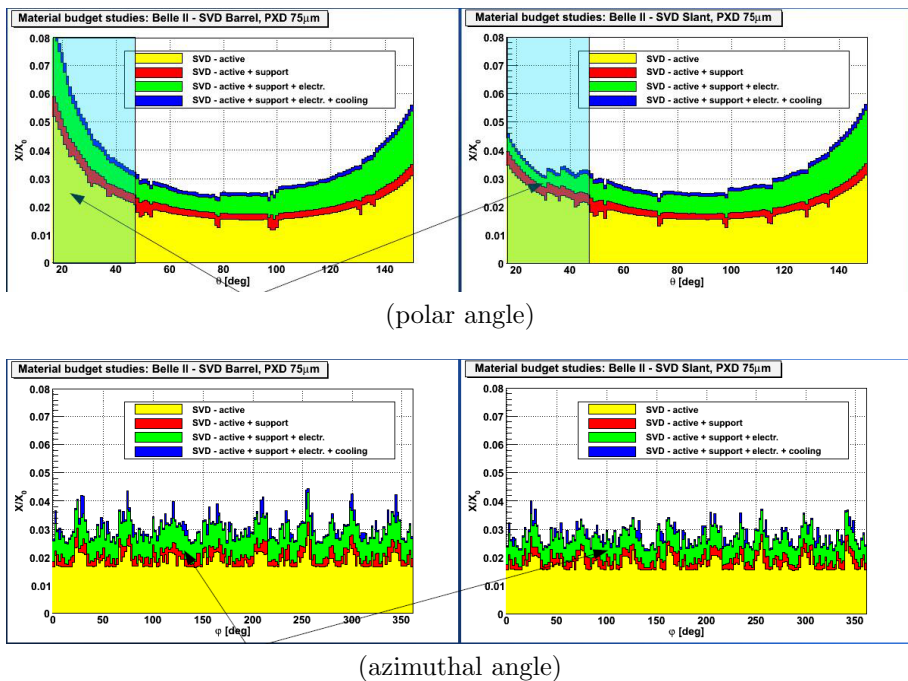


Figure 4.2: Distribution of expected materials as a function of polar angle (top) and azimuthal angle (bottom) for straight (left) and slant (right) design. SVD sensors, support, electronics, and cooling component are considered [3].

4.2 Tracking resolution simulation with fast simulation

4.2.1 TRACKERR simulation

We estimate the vertexing and tracking resolution with TRACKERR [24]. TRACKERR is a FORTRAN based program which enables us to calculate tracking errors easily with simple simulation. TRACKERR first generates a track and hit position at implemented detectors from the input particle and uniform solenoid magnet. Here TRACKERR assumes a helical trajectory. This trajectory is not modified by energy loss. This is the main limitation of this program. We can input only one particle with fixed polar angle and momentum. Each of the hits are then smeared by material, multiple scattering and energy loss, and also smeared by implemented detector resolution. The error matrix is propagated from the end of the track to the inner most layer or to the origin to estimate the impact parameter resolution.

4.2.2 Helix parameters

A charged particle in the uniform magnetic field follows a helical trajectory. There are many ways to parametrize a helical track. The following parametrization is used for track fitting by the Belle data analysis [25]. If z-axis is in the direction of the magnetic field, the trajectories can be written as Eq.(4.1)

$$\begin{aligned} x &= x_0 + dr \cos \phi_0 + \frac{1}{cBQ\kappa} (\cos \phi_0 - \cos(\phi_0 + \phi)), \\ y &= y_0 + dr \sin \phi_0 + \frac{1}{cBQ\kappa} (\sin \phi_0 - \sin(\phi_0 + \phi)), \\ z &= z_0 + dz - \frac{1}{cBQ\kappa} \tan \lambda \cdot \phi, \end{aligned} \quad (4.1)$$

where (x_0, y_0, z_0) is the origin, B is the magnetic field, and Q is the charge. If the origin is fixed, the helix is determined by 5 parameters dr , dz , ϕ_0 , κ , and $\tan \lambda$, where dr is the distance of the trajectory from the origin in the x-y plane, dz is the distance of the trajectory from the origin in the z direction, ϕ_0 is the azimuthal angle to specify the origin with respect to the center of the helix, κ is the signed inverse of transverse momentum $\kappa = 1/p_t$, and $\tan \lambda$ is tangent of the polar angle. The trajectory in the x-y plane and the meaning of the parameters are shown in Figure 4.3, where radius of helix $\rho = 1/cBQ\kappa$. TRACKERR outputs the resolution of these parameters. In this simulation, the interaction point is chosen as the origin. The impact parameters are described as dr and dz . The resolution of impact parameter measurement corresponds to the resolution of dr and dz .

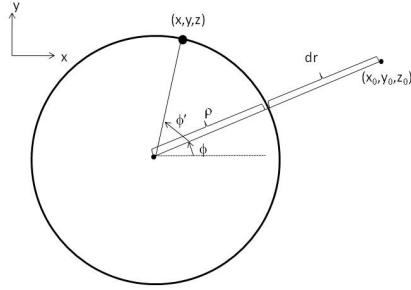


Figure 4.3: A helical trajectory in x-y plane.

4.2.3 Effect on particle through matters

In TRACKERR, multiple scattering and energy loss are taken into account. Here is a brief review of these effects.

- Multiple scattering

Charged particles through matter change their direction by multiple scattering which is mainly result from Coulomb scattering. The angular distribution of the scattering is represented by the Molière equation. This distribution is roughly approximated by gaussian distribution though Molière equation have much larger tail. The best gaussian representation is given by [26]

$$\sigma = 13.6 \text{ MeV} \frac{z\sqrt{X/X_0}}{\beta cp} [1 + 0.088 \log_{10}(X/X_0)], \quad (4.2)$$

where σ is the RMS of the scattering angle, z , p , and βc are the charge, momentum and velocity of the incident particle, X is the thickness of the material, and X_0 is the radiation length.

- Energy loss

Charged heavy particles with moderately high energy through matter lose their energy by ionization. The mean energy loss is described by Bethe-Bloch formula,

$$-\frac{dE}{dx} = 4\pi N_A r_e^2 m_e c^2 Q^2 \frac{Z}{A} \frac{1}{\beta} \left[\frac{1}{2} \ln \frac{2m_e c^2 \beta^2 \gamma^2 T_{max}}{I^2} - \beta^2 \right], \quad (4.3)$$

where N_A is the Avogadro's number, m_e and r_e is the mass and the classical radius of electron, Q , Z , and A are the charge, atomic number, and atomic mass of the material, T_{max} is the maximum kinematic energy, and I is the effective ionization potential. Experimental measurement of ionization potential is available in [27]. In the TRACKERR simulation, I is roughly calculated by $I = 16Z^{0.9}$ as is shown in [28]. The energy loss by ionization doesn't depend on the mass of ionizing particles but on their velocity and intermediate material. Atomic number and radiation length of the material used in my simulation are listed in Table 4.1. ([29]).

	Z	X_0 (g cm $^{-2}$)	$X / X_0 (\times 10^{-3})$
PXD sensor(Si, 75 μm)	14	21.82	0.8
SVD sensor(Si, 300 μm)	14	21.82	3.2
Au plating(10 μm)	79	6.46	3.0
Be pipe(1 mm)	4	65.19	2.83
PF200 coolant(1 mm)	5.28	44.18	1.77

Table 4.1: Atomic number, radiation length and effective thickness of each component(X/X_0). PF200 is the coolant used in CLEO which may have similar physics property to the paraffin used in the Belle system

4.2.4 Intrinsic resolution

The geometrical resolution of the detector is $1/\sqrt{12}$ of a strip pitch or a pixel size [30]. In the case of the SVD, however, one charged particle makes signals for multiple strips and make a cluster. The hit position is determined by center of charge deposit for all strips in the cluster. Therefore, the resolution of the SVD is better than geometrical resolution. The resolution taking into account this effect is called as "intrinsic resolution".

To determine the expected resolution, several simulation studies were performed by Z. Drasal (Figure 4.4)[3]. The dz resolution towards 90 degree get worse because of increase of probability of single-strip events and thus hit points aren't corrected by neighboring strips.

In the forward region the slant design has better dz resolution because, in the case of the straight design, low incident particle angles result in bigger cluster size and thus worse intrinsic resolution. We use this resolution as the input parameter of TRACKERR.

4.2.5 Input parameters

Input parameters for the simulation are shown as follows.

- Detectors
 - PXD
- Two silicon pixel detectors with thickness 75 μm are implemented

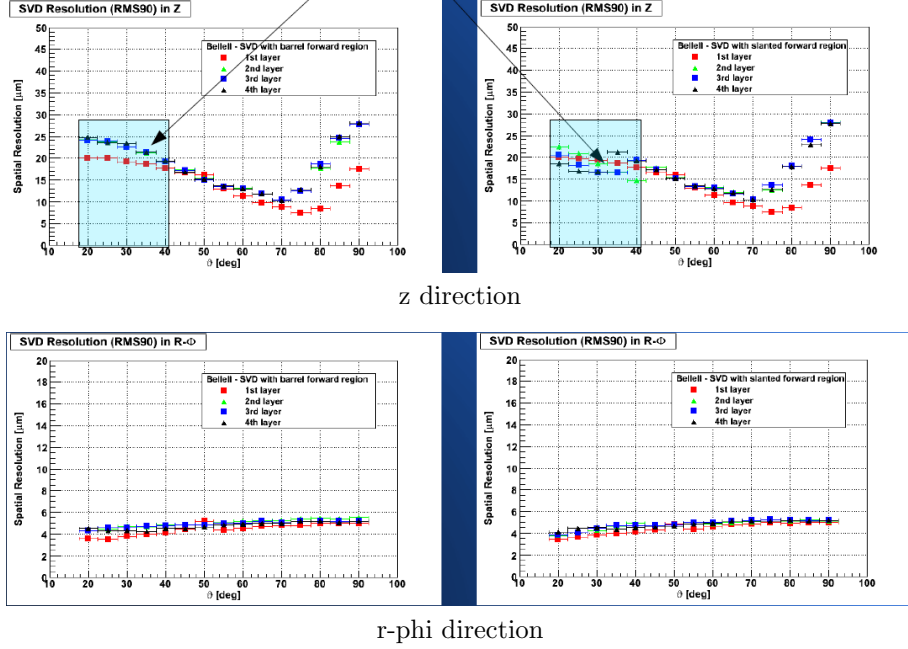


Figure 4.4: Expected intrinsic resolution in z and phi direction[3].

as simple cylindrical shape. The first layer is $50\mu\text{m} \times 50\mu\text{m}$ pixels located at $r = 1.4\text{ cm}$. The second layer is $75\mu\text{m}(z) \times 50\mu\text{m}(r\text{-phi})$ pixels located at $r = 2.2\text{ cm}$. The resolution of each PXD layer is implemented as $(\text{pixel size})/\sqrt{12}$.

– SVD

4 double sided silicon strip detectors (DSSDs) with thickness $300\mu\text{m}$ are implemented as a simple cylindrical shape for barrel part and a cone shape for the forward region of outer three layers of the slant design. The resolution of the SVD is the expected intrinsic resolution discussed in section 4.2.4.

– CDC

The Belle II CDC is implemented as a simple cylindrical shape. The CFRP wall separating the SVD and CDC is also implemented. CDC resolution of each layer is $150\mu\text{m}$.

- Beam pipe

The beam pipe of $r = 1.0\text{ cm}$ comprised by the Beryllium tube, $10\mu\text{m}$ gold plating, and 1 mm Paraffin coolant is implemented as a cylindrical shape.

- Solenoid

Uniform 1.5 T magnetic field is implemented.

- Particle

Incident particle is a pion with momentum from 0.2 to 2 GeV/c. The polar angle of the track is from 20° to 35° in order to cover the slanted region(17° - 30°).

4.2.6 Simulation check

We run TRACKERR and check the behaviour of the simulation. As the first step, we check the dr and dz resolution for each momentum when the particle trajectory is perpendicular to the z direction. In this case, impact parameter resolution should be asymptotically the same as the measurement error of 1st layer of the PXD ($50 \mu\text{m}/\sqrt{12} \sim 14 \mu\text{m}$) in high momentum and be degraded by the effect of multiple scattering at low momentum. The difference between slant and straight design should be very small because there are only tiny difference in detector setting(at location of 4th layer) in this direction. The result is shown in Figure 4.5. The calculated dr resolution is $12.5 \mu\text{m}$ and dz resolution is $14 \mu\text{m}$ at 3GeV/c. These are consistent with the expectation that these resolutions are dominated by the resolution of the innermost PXD($\sim 14 \mu\text{m}$). The momentum dependence of dr and dz resolution shown in Figure 4.5 is also as expected.

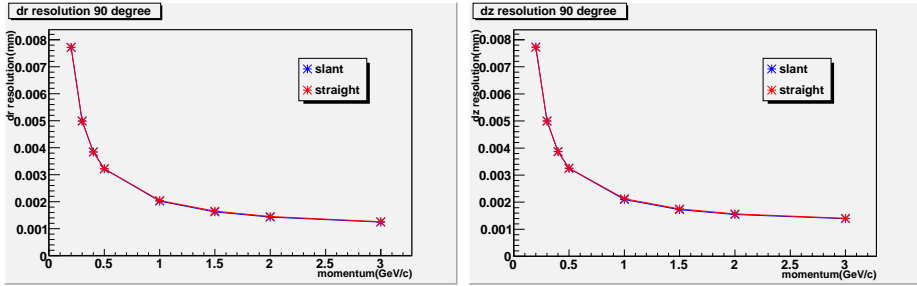


Figure 4.5: Resolution of dr (left side) and dz (right side) when polar angle = 90° . Blue line indicate slant and red line indicate straight design. The horizontal axis is the total momentum. Blue line is almost hidden by red line because the difference between slant and straight design is very small.

The second step is to see the magnet field dependence of the transverse momentum(p_t) resolution. In a stronger magnetic field, the radius of helix become small which results in better p_t resolution in the case of high momentum. On the other hand, in the case of low momentum, the particle can't reach all detectors and hit number decreases in a stronger magnetic field which results in worse p_t resolution. The results for $B = 1.5$ and 1.2 T are shown in Figure 4.6. We find better p_t resolution in a stronger magnetic field at higher momentum and in a weaker magnetic field at lower momentum which is consistent with the expectation. After these checks, we confirm that TRACKERR runs correctly.

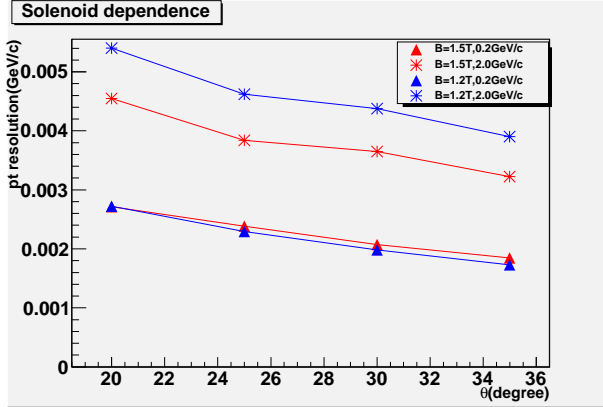


Figure 4.6: Resolution of p_t when solenoid magnetic field change. Red lines indicate 1.5 T and blue lines indicate 1.2 T. Each marker style indicates the particle momentum (Δ : 0.2 GeV/c, $*$: 2.0 GeV/c). The SVD configuration is slant design. The horizontal axis is the polar angle.

4.2.7 Effect of paraffin coolant

We study the effect of thickness for paraffin coolant in the beam pipe. This is related to the design of the cooling system because the return cooling system (See chapter 3) requires twice the paraffin gap if we want to operate with the same flow rate. Figure 4.7 shows the effect of additional 500 μm of paraffin on impact parameter and p_t resolution. The impact parameter resolution is degraded by 6% (at 0.2 GeV/c) or less than 1% (at 2 GeV/c) and also p_t resolution is degraded by 3% by additional 500 μm of paraffin. The material of the beam pipe greatly affects the impact parameter resolution because there is no detector inside the beam pipe. Thickness of cooling gap can have impact on the physical result. We should try to decrease the thickness as much as possible, while keeping enough cooling power.

4.2.8 Estimation of vertexing and tracking performance

The vertex (dr, dz) resolution and transverse momentum resolution for the very forward region are calculated to compare two SVD designs.

Figure 4.8 is the impact parameter resolution in the forward region. The difference in the outer layer is not significant because the impact parameter resolution depends much on inner most layer. Even at low momentum (0.2 GeV/c), the slant design has less than 1% better resolution compared to the straight design.

If the hit finding efficiency of the PXD is perfect, we can determine the position accurately. In very high occupancy environment, however, hit finding efficiency is degraded. In this case, good position resolution of the SVD is

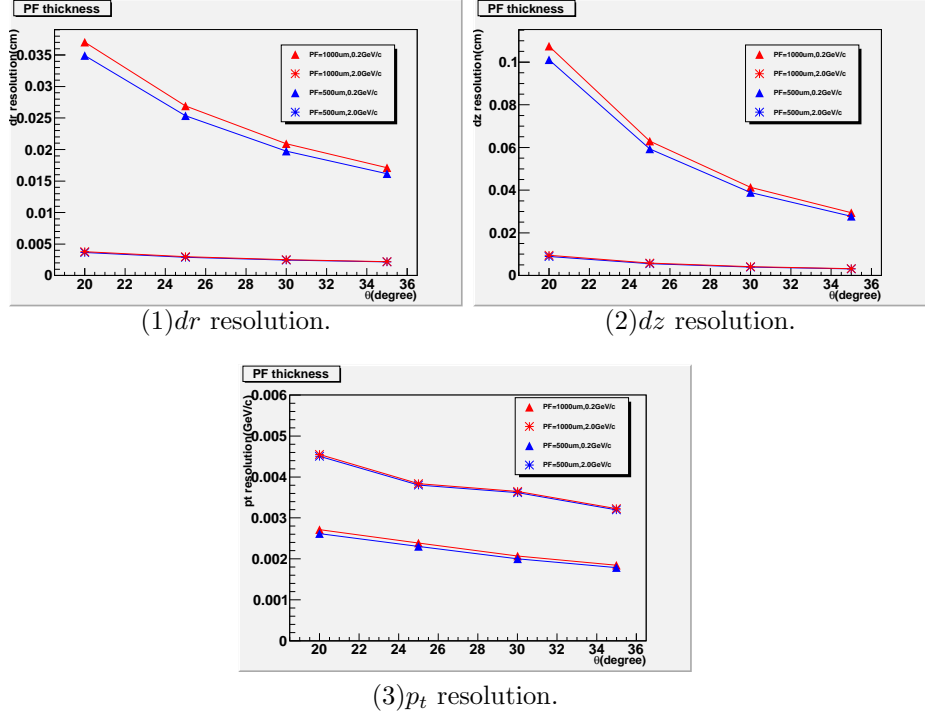


Figure 4.7: Effect of the paraffin gap thickness on tracking parameters. Red lines indicate 1 mm paraffin and blue lines indicate 500 μm . Each marker style indicates the particle momentum (\triangle :0.2 GeV/c, $*$:2.0 GeV/c). The SVD configuration is slant design. The horizontal axis is the polar angle.

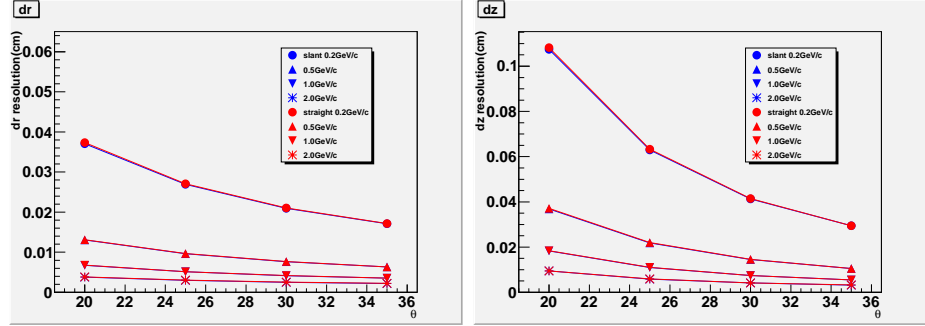


Figure 4.8: Resolution of dr (left side) and dz (right side). The horizontal axis is the polar angle. Blue lines indicate slant and red lines indicate straight design. Each marker style indicates the particle momentum (\circ :0.2 GeV/c, \triangle :0.5 GeV/c, ∇ :1.0 GeV/c, $*$:2.0 GeV/c).

required. In this simulation, the effect of the beam background is not taken into account and degradation of hit finding efficiency is not studied. To simply study for high occupancy experiment, we also simulate the SVD and the CDC only configuration, without the PXD (Figure 4.9). In this case, though the slant design has better resolution than straight design, the difference is less than 2% (dr) or 1% (dz). The SVD and the PXD are also able to reconstruct K_s mesons that decay not at the IP but outside the PXD. Although the reconstruction performance of K_s is not simulated in this study, the good resolution of SVD is required to measure the decay point of K_s accurately.

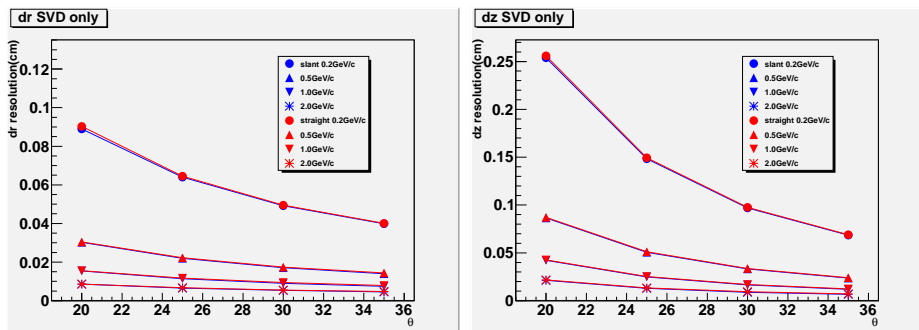


Figure 4.9: Resolution of dr (left side) and dz (right side) without the PXD. The horizontal axis is the polar angle. Blue line indicate slant and red line indicate straight design. Each marker style indicates the particle momentum (\circ :0.2 GeV/c, \triangle :0.5 GeV/c, ∇ :1.0 GeV/c, $*$:2.0 GeV/c).

Figure 4.10 shows transverse momentum resolution of the configuration both with and without the PXD. The p_t resolution is mainly dependent on the length of the lever arm, distance between innermost and outermost layer, which is mainly determined by the CDC. The slant design has better resolution than straight design because of less multiple scattering. The difference between the two designs is 6% or less for configuration with the PXD. In the case of configuration without the PXD, the difference is also 6% or less.

4.3 Comparison with the result of 2004

In 2004, the impact parameter resolution of the SVD and PXD was estimated using TRACKERR (this result is shown in [4]).

We compare result of 2010 with that of 2004. The difference between the condition of 2004 and 2010 study is the detector configuration. Two silicon pixel detectors are also implemented in the condition of 2004 study but details are not same. The first layer has $50\mu\text{m}(z) \times 400\mu\text{m}(r\text{-phi})$ pixels located at $r = 1.3$ cm and the second layer has $400\mu\text{m}(z) \times 50\mu\text{m}(r\text{-phi})$ pixels located at $r = 1.5$ cm. These pixels are larger than the assumed pixel size in the 2010 study. Moreover the effective thickness is larger ($300\mu\text{m}$). Because of these differences,

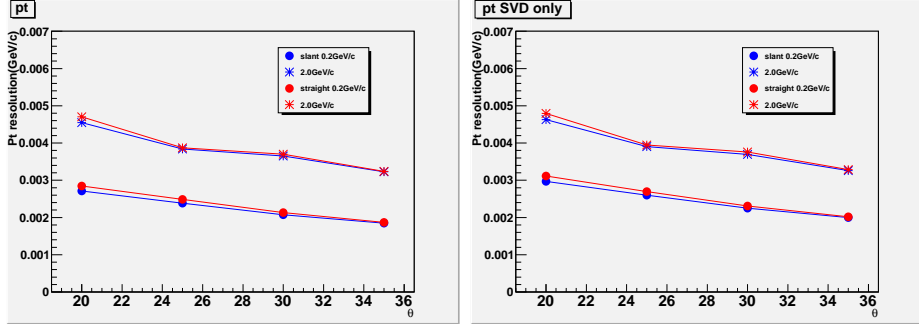


Figure 4.10: Resolution of transverse momentum of SVD+CDC+PXD (left side) and SVD+CDC (right side). The horizontal axis is the polar angle. Blue lines indicate slant and red lines indicate straight design. Each marker style indicates the particle momentum (\circ :0.2 GeV/c, $*$:2.0 GeV/c).

the estimated impact parameter resolution of the 2004 study is expected to be worse than the 2010 study and better than the 2010 study without the PXD.

The impact parameter resolution of the 2004 study and 2010 study are shown in Table 4.2. Because the region only from 30° to 150° is simulated in 2004, we can compare these results only at 30° . The resolution of the slant design of the 2010 result is better than the 2004 result because of smaller pixel size. On the other hand, the 2004 result is better than the condition of the slant SVD without the PXD in the 2010 result. All these results agree with the expectation.

	2004	2010 (slant)	2010 (slant without PXD)
$\Delta dr(\mu\text{m})(0.2\text{GeV}/\text{c}, 30^\circ)$	325	210	490
$\Delta dz(\mu\text{m})(0.5\text{GeV}/\text{c}, 30^\circ)$	210	150	330

Table 4.2: The dr and dz resolution of 2004 and 2010 result.

4.4 Summary

We estimate the tracking performance of the SVD with TRACKERR simulation. At first, we study the effect of thickness of paraffin coolant. The impact parameter resolution is degraded by 6% or less and also p_t resolution is degraded by 3% by additional 500 μm of paraffin.

Next, we simulate the difference in tracking performance between slant and straight design. The slant design has a better impact parameter resolution (<2%) and p_t resolution (<6%). So far, we don't mention the angular distribution of decay particles. In the real experiment, few particles are expected to hit at the forward region and effect of difference in this region is expected

to be small. In this simulation, background is not also taken into account. If background-origin hit exist, they will degrade the track reconstruction performance. To estimate these effects, full simulation with GEANT4 and track-finding codes are being prepared.

At the Belle II general meeting in 2010 November, after some discussions, including this simulation study, SVD group decided to choose the slant design as a base line option. We keep working on more realistic studies including structure design, full simulation, fixed-type mask design, etc... based on this decision.

Chapter 5

Conclusion

We estimated the Touschek and beam-gas background levels at SuperKEKB. Here are three assumptions in this estimation. One is that beam loss particles generate the same level background as the Belle case. This means that we use the same proportional constant k . Next, beam loss by beam gas is assumed to be the same as KEKB. Finally, beam loss by Touschek can be estimated by optics simulation. The occupancy of the Belle II SVD and PXD is estimated to be 6.6% and 2.0% respectively. The hit rate of the Belle II CDC is estimated to be less than 84 kHz/wire. The background of Belle II TOP is expected to correspond to the background level which causes a trigger rate of 2.9 MHz in the Belle TOF. The total energy deposit of particle hits above 1 MeV at the ECL is expected to be less than 1.5 MeV/trigger/crystal on average. The estimated background level of the SVD, CDC, and ECL are within the tolerable levels under the estimated background condition. Other kinds of background, such as synchrotron radiation or QED background are being estimated separately.

We checked the cooling capability of the beam pipe with paraffin ($N=10$) coolant. It is concluded that we can circulate paraffin through a return cooling system at 1.8 l/min with a pressure drop of <0.1 MPa. 1 l/min flow of coolant is enough to remove the expected ~ 80 W of heat. The expected temperature difference between the entrance and exit of the coolant is ~ 2.5 °C. We are now thinking of choosing a beam pipe with a one-way cooling system using paraffin. The one-way cooling system is expected to have better cooling capability at the forward end than the return cooling system. In this design, the forward manifold doesn't conflict with the PXD. The one-way design requires less paraffin thickness to achieve the same flow rate than the return cooling system which enables us to improve the tracking parameter resolution by 6% or less. The cooling capability of the one-way cooling system will be checked with a stainless steel mockup.

We performed a simulation study to understand the difference in the tracking performance between slant and straight designs of the SVD outer layers. It was concluded that the slant design has better impact parameter resolution (<2%) and p_t resolution (<6%). We decide to adopt the slant design as a base line

option. We still have to estimate background for the SVD and manage space for the heavy metal shield if necessary.

A current design of the IR is shown in Figure 5.1 Even after this intensive study, several issues still remain to be resolved in the IR. For example, we have to optimize the position of the fixed-type and movable masks to reduce beam background. A continued effort will be necessary to cope with extremely high backgrounds to ensure the success of the Belle II experiment.

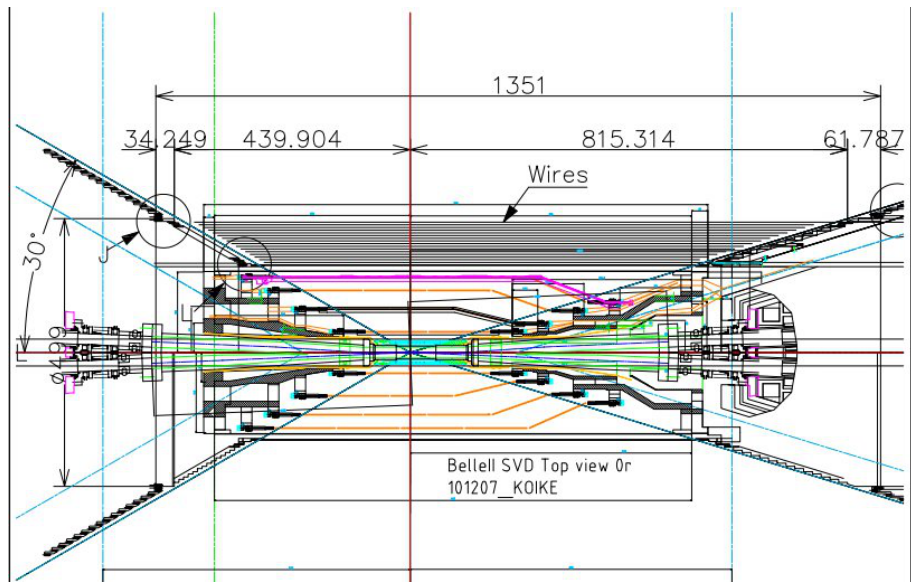


Figure 5.1: Schematic design of Belle II interaction region.

Appendix A

Miscellaneous topics about Touschek study

A.1 Mask setting dependence

We conducted a beam test at different mask settings to study mask setting dependence of beam background. The mask settings are both horizontal and vertical masks open, vertical masks close and horizontal masks open, and vertical masks open and horizontal masks close. At each mask setting, the vertical beam size is scanned in order to separate the contribution from the Touschek effect and other backgrounds. The Vertical beam size is changed by changing i-size-bump (See section 2.4.1). The life time and background increase as the beam size decreases. The study is performed for only the LER. Figure A.1 shows the mask condition dependence of CDC background. The horizontal axis is the inverse life time and the vertical axis is the CDC current normalized by the beam current. The beam current is 1450 mA.

From Eq.(2.1), CDC current per beam current is expected to be proportional to $1/\tau$ and fitted by a linear function. In the red plot, however, the plot seems to bend at $1/\text{life} = 0.006/\text{min}$. We don't expect this behavior. A possible explanation is that with larger beam size the beam bunch grazes at the edge of the mask and cause showers so that background increase and slope of the plot becomes larger. Comparing the red plot and the other plots, it is found that both horizontal and vertical masks reduce beam background.

A.2 Beam current dependence

We conducted a beam test at different beam currents to study bunch current dependence of beam background. In each run, beam current is set at 1450 mA, 1100 mA, and 750 mA. At each beam current, the vertical beam size is scanned in order to separate the contribution from the Touschek effect and other back-

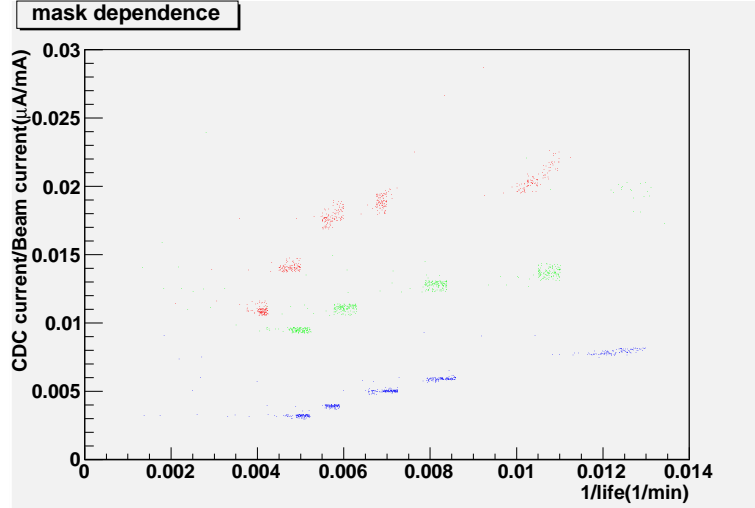


Figure A.1: Movable mask dependence of CDC current per beam current at the LER. Red:both open (Run 574). Blue:vertical masks close, horizontal masks open (Run 567). Green:vertical masks open, horizontal masks close (Run 575). The beam current is 1450 mA, the ring is the LER.

grounds. The study is performed for only the LER. The life time and background increase as the beam size decreases. Figure A.2 shows the beam current dependence of CDC current normalized by beam current during the beam test. Beam current is varied by changing bunch current, while the number of bunches is constant. The horizontal axis is the inverse life time and the vertical axis is the CDC current divided by the beam current. Both horizontal and vertical masks open condition (see section 2.4.1) is used.

As is seen in section 2.4.2, $\text{Background}_{\text{Touschek}}$ is proportional to I_{bunch}^2 and $\text{Background}_{\text{beam-gas}}$ is proportional to I_{bunch} . If the inverse life time dependence of background can be fitted by a linear function, which is expected by the simple assumption of Eq.(2.1), that the difference between each current condition in the slope of the line is the effect of current dependence of $\text{BG}_{\text{Touschek}}$ and in the offset is the effect of current dependence of $\text{BG}_{\text{beam-gas}}$.

We again find bending effect at inverse life $\sim 0.006/\text{min}$. However, as we don't fully understand bending structure, precise analysis is not easy.

A.3 Number of bunch dependence

We conducted a beam test at a different number of bunches while keeping the bunch current unchanged to study number of bunch dependence of beam background. At each number of bunch condition, the vertical beam size is scanned

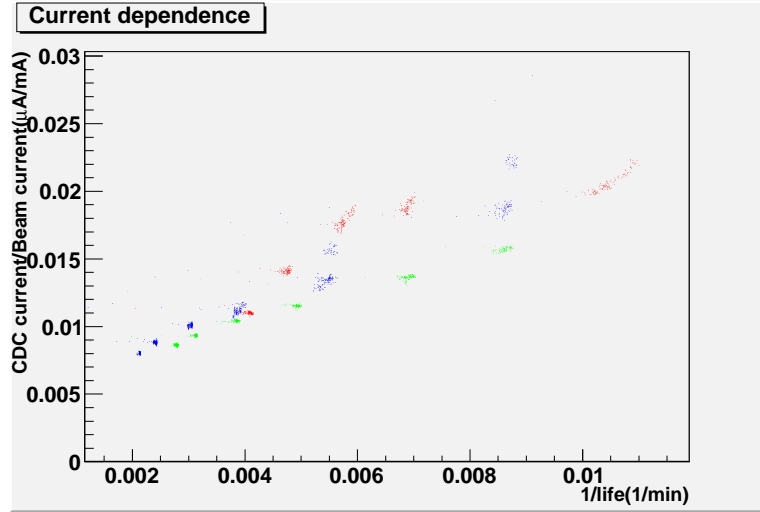


Figure A.2: Beam current dependence of CDC current per beam current at the LER. Red:1450 mA (Run 574). Green:1100 mA (Run 577). Blue:750 mA (Run 576). The mask setting is both open.

in order to separate the contribution from the Touschek effect and other backgrounds.

Figure A.3 shows the number of bunch dependence of CDC background at the LER. The horizontal axis is the inverse life time and vertical axis is the CDC current divided by beam current (proportional to the bunch number). Mask setting is open for both horizontal and vertical. The red plot is for the default bunch number and blue plot is for the half number of default setting.

As is seen in section 2.4.2, both $\text{Background}_{\text{Touschek}}$ and $\text{Background}_{\text{beam-gas}}$ are proportional to the number of bunch. The background level normalized by number of bunches seems to be consistent to first order. This confirms that beam life time is proportional to the number of bunches, and our result agrees with the expectations.

Bending effects are again found at inverse life $\sim 0.006/\text{min}$. We don't fully understand bending structure, precise analysis is not easy.

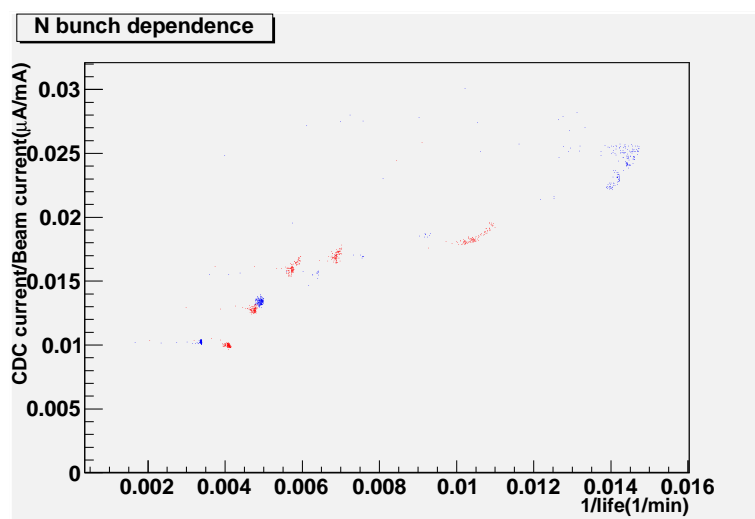


Figure A.3: Bunch number dependence of CDC current per beam current at the LER. Red:bunch number = 1585 (Run 574). Blue:bunch number = 796 (Run 580). The mask setting is both open.

Appendix B

Vacuum bump study

B.1 Beam gas background at the IP

The vacuum level of the ring part of SuperKEKB is expected to be as same as current KEKB. On the other hand, the vacuum level of the IP is expected to be 100 to 1000 times worse than at present. Here beam loss by beam-gas scattering is very high though lost particles are expected to pass through towards downstream and not to have negligible effect on detector as background. To understand effect of this extremely degraded vacuum at the IP, we performed a beam test in Dec. 2009. In this study, we change the vacuum level at the IP by stopping the ion pump and turning on the Non Evaporable Getter (NEG) pump. Figure B.1 shows the CDC current, beam life time, and vacuum level of the IP. We find that the life time gets smaller as the vacuum level at the IP gets worse, however, CDC current is still unchanged. It is confirmed that beam-gas background due to degraded vacuum level at the IP can be neglected.

B.2 Vacuum bump study at upstream of the IP

We operated beam test called vacuum bump study. This study is aimed to estimate $k_{beam-gas}$, which is defined in chapter 2, by changing vacuum level. We changed the vacuum level at upstream of the IR for the HER and the LER. We set movable masks as vertical close and horizontal open setting. Table B.1 shows the run summary of vacuum bump study.

At first, ion-pump at the corresponding region is off. Then for only D1 or D2 region, very close to the IR, NEG pumps are on. During the run, we monitored the CDC current and operate without down the DAQ system.

Figure B.2 shows the CDC current, beam life time and vacuum pressure at D1 region during changing vacuum level at D1 region. We find smaller life time and more background at the CDC ascribe to greater beam-gas scattering caused by degraded vacuum. The relation between CDC current scaled by beam current and inverse life time is shown in Figure B.3. To determine the data point and

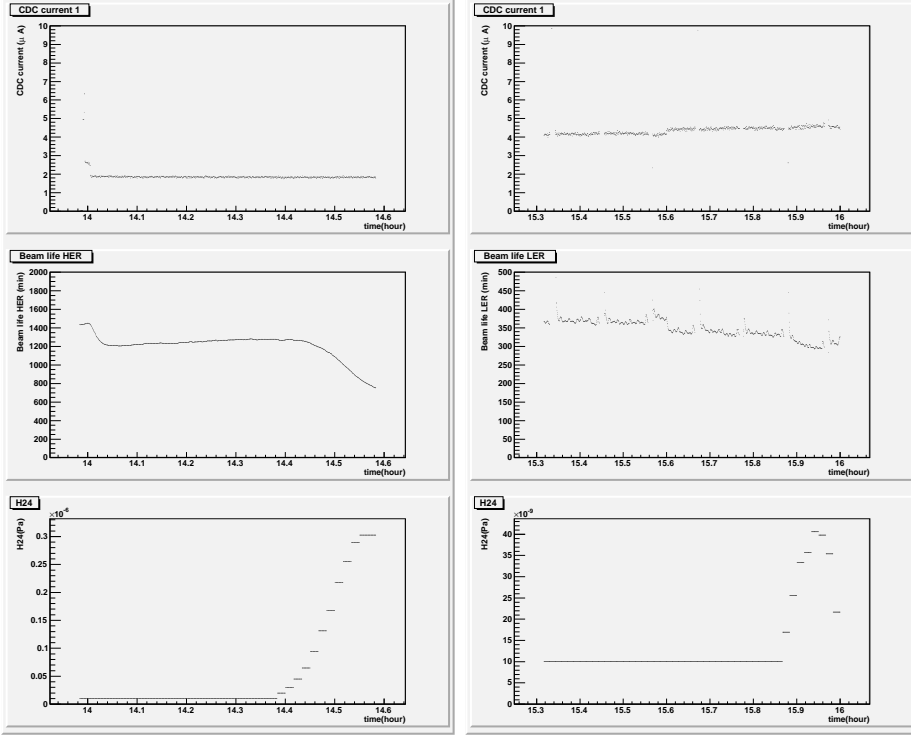


Figure B.1: CDC current (top), beam lifetime (middle) and vacuum of the IP (bottom) during IP vacuum bump study of HER (left) and LER (right). The horizontal axis of all graphs are time (hour).

run No.(Exp. 73)	time	bump region	ring
854	18:49-18:54	D12	HER
854	18:58-21:10	D1	HER
856	22:40-22:48	D3	LER
856	22:56-23:51	D2	LER

Table B.1: Summary of vacuum bump study.

the error of the point, the data are divided at the same interval of the inverse life time. The data point is the mean value of each divided data set. The error of the data point is at first calculated as $\text{RMS}/\sqrt{\text{entries}}$ and then it is scaled so that the reduced χ^2 become unity. We fit the data by linear function. The slope of this fitted function is $k_{beam-gas}$. The $k_{beam-gas}$ based on this information is estimated to be $50 \pm 1 \mu\text{A}*\text{min}/\text{mA}$ and $8.5 \pm 0.5 \mu\text{A}*\text{min}/\text{mA}$ for HER and LER respectively. These values are much larger than obtained in section 2.5.3. This is because we change vacuum pressure at only one region of whole ring. In real beam run, scattering by beam-gas effect happens at whole ring and few of scattering particles become background in the detector. However in this study, beam loss is mainly at near upstream of the IP and many scattering particle hits produce detector background. To make a more precise expectation, we evaluate $k_{beam-gas}$ by other methods using "Touschek study" data (section 2.5.2).

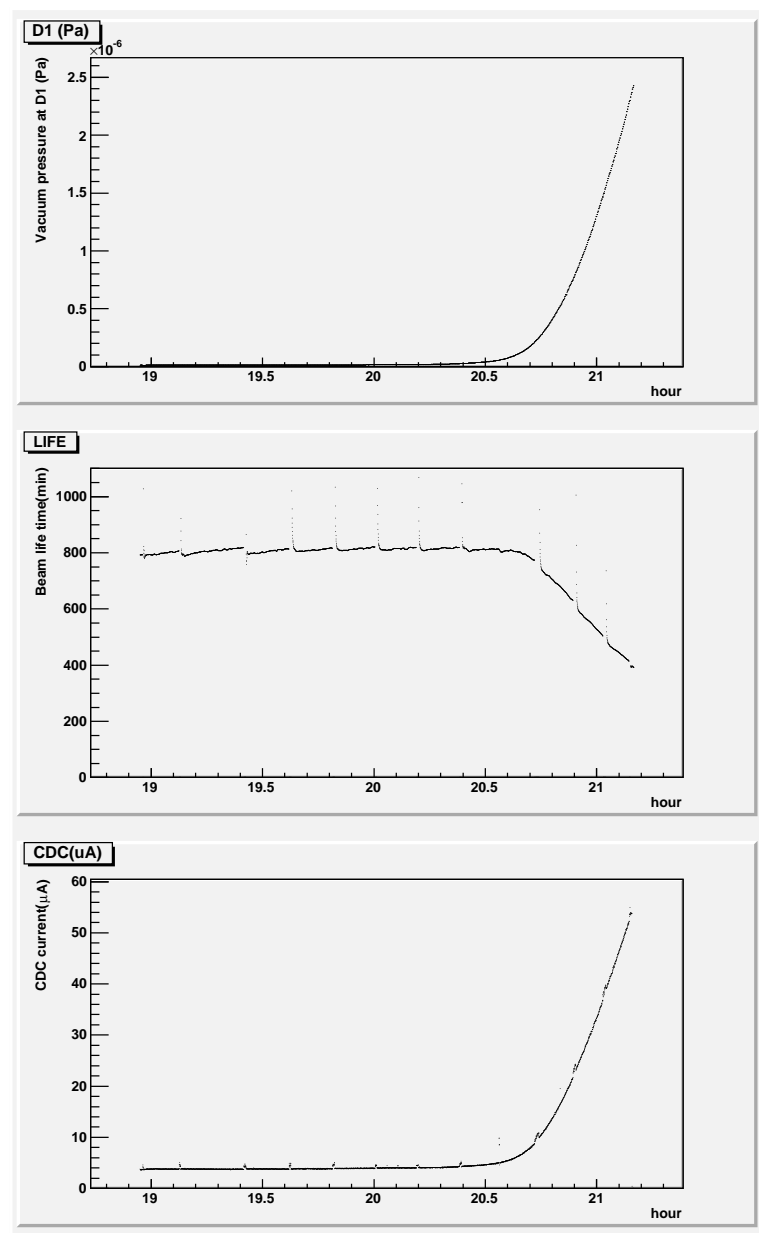


Figure B.2: Vacuum pressure at the D1 (top), beam life time (middle) and CDC current (bottom) for the HER. The horizontal axes of all graphs are time (hour).

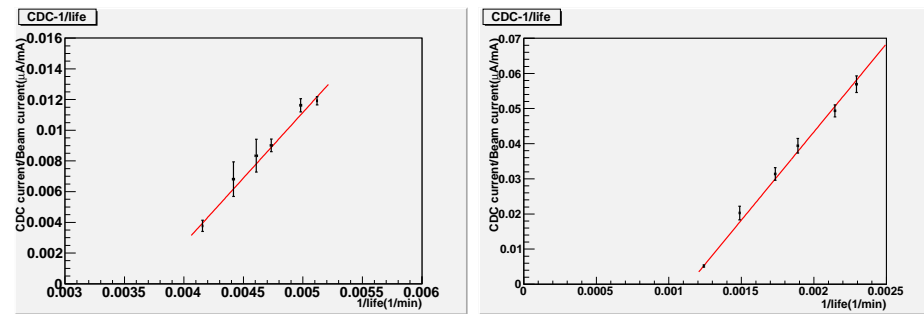


Figure B.3: CDC current normalized by beam current versus beam life time for the HER (left) and the LER (right) when vacuum level at upstream of the IR changed.

Appendix C

KEKB beam background simulation check

To estimate Touschek and beam-gas background at SuperKEKB, a simulation study was performed by H. Nakano [6]. In the first step of his study, Belle detector simulation is performed to confirm the simulation frame work validity. SVD occupancy of the Belle SVD is estimated by the simulation and compared with real beam test data taken in beam test performed in the "Touschek study" (See section 2). In this chapter, we present calculation of the Belle SVD occupancy with the Touschek study data.

C.1 KEKB simulation for Touschek and beam-gas background estimation.

To estimate Touschek and beam-gas background at SuperKEKB, a simulation study is performed. At the first step, a simulation study of the KEKB accelerator and the Belle detector is performed and checked for validity. Background at SuperKEKB and Belle II is simulated after the check.

This simulation is based on TURTLE and a GEANT3 based Belle full simulator. At first TURTLE simulates KEKB ring from down stream of the IP to other side of the IP. The incident particle is generated with randomly generated emittance and phase space (x, x', y, y') by gaussian distribution. At the beginning of the simulation, TURTLE decides where the particle interacts by bremsstrahlung, Coulomb scattering or Touschek effect. The particle is then transported to that point through beam line changing its position and momentum by matrix calculation. At the scattering point, its momentum and position are changed according to the distribution of scattering angle or energy for each interaction. After the scattering, particle is transported again.

At the end of the simulation, particle's position and momentum are taken over to the Belle full simulator. The particles are transported by the GEANT

tracking routines. The information of SVD hit with >3000 electron-hole pairs (~ 10 keV) is stored in the simulation. To check the simulation, SVD occupancy of inner 3 layers caused by each background source at Belle is estimated.

C.2 SVD occupancy measurement

SVD occupancy estimated in section C.1 is comparable to beam test, Touschek study, because the background from each effect is measured for each ring as is discussed in chapter 2. The method to evaluate the SVD hit at Belle from Touschek study data is shown in section 2.4.2 and section 2.5.4. The life time of Touschek at Belle is estimated from Figure 2.6. Assuming that the vertical beam size is $2 \mu\text{m}$, the life time of Touschek at Belle is 130 min for LER and 1300 min for HER. The life time of beam-gas, k_{Touschek} , and $k_{\text{beam-gas}}$ of each SVD layer is evaluated. In this evaluation, the value we call "beam-gas" is actually the value for "no Touschek effect" and may include not only beam-gas background but other background such as synchrotron radiation hits.

Some strips have a base signal around 3.5×10^5 eV at the outer layers of the SVD (Figure C.1). This is considered as electric noise. In my analysis, strips which have 5 times higher signal rate than the average of the each layer are excluded. No strips in the 1st layer, 23 strips in 2nd layer and 167 strips in 3rd layer are excluded by this analysis. After this exclusion, we calculate SVD occupancy with energy >3000 electron-hole pairs.

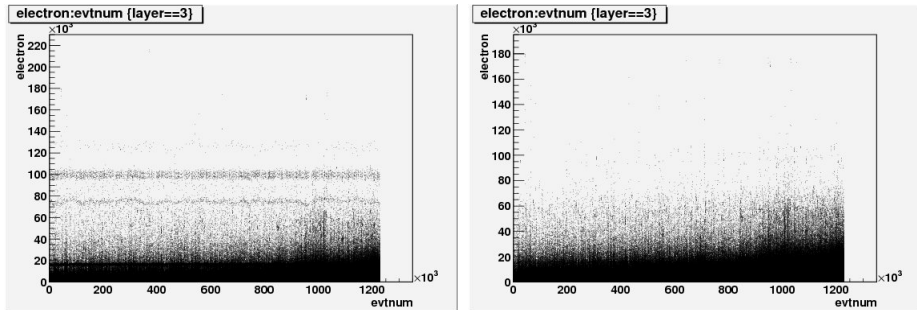


Figure C.1: Hits at around 4×10^5 eV at the 3rd layer of the SVD before (left) and after (right) excluding electric noise. Horizontal axis is the event number. Vertical axis is the number of electron-hole pairs. One electron-hole pair corresponds to 3.6 eV.

C.3 Results

The results are shown in this section. Assumed beam parameters in the simulation and the beam test are shown in Table C.1. The vacuum pressure varies with location of the beam line. For example, vacuum level at the injection

	simulation	beam test
Beam current(HER/LER)(mA)	1188/1637	850/1450
σ_y (μm)	2	2
σ_x (μm)	200	200

Table C.1: Parameters for the simulation and the beam test

septum magnet or wiggler magnet($\sim \text{O}(10^2)$ nPa) are worse than the other area($\sim \text{O}(10^1)$ nPa). The position dependence of the pressure is checked according to the 300 pressure gauge values located at whole KEKB ring. The occupancy estimated by the simulation is scaled by beam current according to the relation of $\text{BG}_{\text{Touschek}} \propto I^2$ and $\text{BG}_{\text{Touschek}} \propto I$ (see section 2.4.2).

The estimated background from the simulation and evaluated background from the Touschek study are shown in the Table C.2. The error of the simulation includes only statistical error. Systematic error is not obtained precisely. For example, vacuum pressure has a systematic error of factor of ~ 10 and beam-gas scattering also has systematic error of factor of ~ 10 . The estimation values by the simulation are consistent with the beam test data by a factor of 3 except for the beam-gas effect from the HER and the Touschek effect on the 3rd layer from the LER.

The beam-gas background from the HER is underestimated by the simulation study. This is because the synchrotron radiation is not simulated in the simulation. The synchrotron radiation power from the LER is smaller than the HER, thus only underestimation of the beam-gas effect is seen in the HER. Synchrotron radiation hit from HER is ~ 10 to 30% of total HER background. Thus, the effect of synchrotron radiation on SVD occupancy is ~ 0.1 to 0.3%. The Touschek effect at the 3rd layer from the LER seems to be overestimated by the simulation study. This is because the GEANT simulation area may have been overestimated.

From above discussion, it is confirmed that the simulation is valid. After this check, simulation study can go to the next step, the simulation of the Belle II detector.

(1st layer)

	simulation(%)	beam test(%)	ring
Touschek	0.52±0.03	0.47±0.07	LER
Beam-gas	0.45±0.05	0.19±0.07	LER
Touschek	0.083±0.001	0.006±0.002	HER
Beam-gas	0.082±0.002	0.49±0.003	HER
Total	1.14±0.06	1.2±0.1	

(2nd layer)

	simulation(%)	beam test(%)	ring
Touschek	0.32±0.01	0.14±0.03	LER
Beam-gas	0.17±0.02	0.06±0.04	LER
Touschek	0.024±0.0003	0.01±0.01	HER
Beam-gas	0.025±0.0005	0.18±0.01	HER
Total	0.54±0.03	0.38±0.05	

(3rd layer)

	simulation(%)	beam test(%)	ring
Touschek	0.74±0.02	0.08±0.02	LER
Beam-gas	0.10±0.01	0.10±0.02	LER
Touschek	0.022±0.0003	0.001±0.01	HER
Beam-gas	0.017±0.0003	0.14±0.01	HER
Total	0.88±0.03	0.33±0.03	

Table C.2: Occupancy of each SVD layer (1-3) estimated by simulation and measured.

Acknowledgement

I would like to express my deepest gratitude to my supervisor H. Aihara.

I am especially to H. Nakayama for his support on my study. I also show my appreciation to H. Kakuno, T. Abe, H. Yokoyama, and M. Iwasaki for their advices.

I especially acknowledge T. Tsuboyama, S. Tanaka and the other member of Belle-II IR group. I am indebted to S. Uno, I. Nakamura, S. Uehara, K. Suzuki, K. Inami for discussion about the Belle-II sub-detectors. I am also indebted to T. Hara for his technical support on my analysis.

I am thankful to the members in Aihara Group: H. Miyatake, H. Fujimori, S. Mineo, C. Ng, and J. Wang.

Finally, I would like to express my gratitude to my parents

Bibliography

- [1] Machine parameters. <http://kds.kek.jp/conferenceDisplay.py?confId=5703>.
- [2] Y. Suetsugu and et al. Latest movable mask system for kekb. *Nuclear Instruments and Methods in Physics Research A* 513, 513.
- [3] Z. Drasal. Slide for 7th open meeting of the belle ii collaboration, Nov. 2010.
- [4] Belle-II collaboration. Letter of intent, Apr. 2004.
- [5] M. Tawada. Oho'04 beam-beam interaction.
- [6] H. Nakano. A simulation study of beam backgrounds at the kekb and super kekb colliders, 2010.
- [7] Y. Ohnishi. Oho'04 luminosity frontier.
- [8] isize feedback. <http://www-acc.kek.jp/kekbn/SupportGroup/KEKB-manual-html/Collision/iSize/iSizeFeedback.html>.
- [9] Y. Funakoshi. Slide for 6th open meeting of the belle ii collaboration, Jun. 2010.
- [10] Private communication with s.uno.
- [11] Belle-II collaboration. Letter of intent, Apr. 2004.
- [12] T. Yamaguchi. Photon background simulation for belle tof. *Belle Note*, 133, 1996.
- [13] Private communication with s.uehara, m. jones and k. hiromichi.
- [14] Belle-II collaboration. Belle ii tdr. Fig. 9.3.
- [15] Belle-II collaboration. Belle ii tdr. Fig. 9.10.
- [16] J. D. Jackson. *Classical Electrodynamics 2nd edition*, page 350.
- [17] A. Chao and M. Tigner. *Handbook of accelerator physics and engineering*.
- [18] babar sad book, 1998.

- [19] D. Cinabro and S. McGee. Studies of coolant compatibility with beryllium. Apr. 1998.
- [20] Viscosity of decane. lechner, m.d. (ed.). springermaterials - the landolt-bornstein database.
- [21] Carl Schaschke. *Fluid Mechanics: Worked Examples for Engineers*, page 86.
- [22] Lechner, m.d. (ed.). springermaterials - the landolt-bornstein database.
- [23] I. GFall. Slide for 7th open meeting of the belle ii collaboration, Nov. 2010.
- [24] W. Innes. Trackerr, a program for calculating tracking errors. *Tech. Rep. SLAC-BABAR-Note*, 121, 1993.
- [25] Y. Ohnishi. Track parametrization. *Belle Note*, 148, 1996.
- [26] G.R. Lynch and O.I Dahl. Approximations to multiple coulomb scattering. *Nucl. Instrum. Methods*, B58:6, 1991.
- [27] Particle Data Group. Passage of particles through matter, 2010. Figure 27.5.
- [28] Konrad Kleinknecht. *Detectors for Particle Radiation 2nd edition*, page 14. Cambridge University Press, 1998.
- [29] D. E. Groom. Atomic and nuclear properties. <http://pdg.lbl.gov/2009/AtomicNuclearProperties>.
- [30] Konrad Kleinknecht. *Detectors for Particle Radiation 2nd edition*, page 42. Cambridge University Press, 1998.